J. Fluid Mech. (2011), *vol.* 686, *pp.* 109–159. © Cambridge University Press 2011
doi:10.1017/jfm.2011.289

The generalized Onsager model for the secondary flow in a high-speed rotating cylinder

S. Pradhan and V. Kumaran†

Department of Chemical Engineering, Indian Institute of Science, Bangalore 560 012, India

(Received 28 February 2011; revised 21 May 2011; accepted 3 July 2011;
first published online 26 September 2011)

The generalizations of the Onsager model for the radial boundary layer and the Carrier–Maslen model for the end-cap axial boundary layer in a high-speed rotating cylinder are formulated for studying the secondary gas flow due to wall heating and due to insertion of mass, momentum and energy into the cylinder. The generalizations have wider applicability than the original Onsager and Carrier–Maslen models, because they are not restricted to the limit $\mathscr{A} \gg 1$, though they are restricted to the limit $Re \gg 1$ and a high-aspect-ratio cylinder whose length/diameter ratio is large. Here, the stratification parameter $\mathscr{A} = \sqrt{m\Omega^2R^2/(2k_BT)}$. This parameter $\mathscr{A}$ is the ratio of the peripheral speed, ΩR, to the most probable molecular speed, $\sqrt{2k_BT/m}$, the Reynolds number $Re = \rho_w\Omega R^2/\mu$, where m is the molecular mass, Ω and R are the rotational speed and radius of the cylinder, k_B is the Boltzmann constant, T is the gas temperature, ρ_w is the gas density at wall, and μ is the gas viscosity. In the case of wall forcing, analytical solutions are obtained for the sixth-order generalized Onsager equations for the master potential, and for the fourth-order generalized Carrier–Maslen equation for the velocity potential. For the case of mass/momentum/energy insertion into the flow, the separation-of-variables procedure is used, and the appropriate homogeneous boundary conditions are specified so that the linear operators in the axial and radial directions are self-adjoint. The discrete eigenvalues and eigenfunctions of the linear operators (sixth-order and second-order in the radial and axial directions for the Onsager equation, and fourth-order and second-order in the axial and radial directions for the Carrier–Maslen equation) are determined. These solutions are compared with direct simulation Monte Carlo (DSMC) simulations. The comparison reveals that the boundary conditions in the simulations and analysis have to be matched with care. The commonly used 'diffuse reflection' boundary conditions at solid walls in DSMC simulations result in a non-zero slip velocity as well as a 'temperature slip' (gas temperature at the wall is different from wall temperature). These have to be incorporated in the analysis in order to make quantitative predictions. In the case of mass/momentum/energy sources within the flow, it is necessary to ensure that the homogeneous boundary conditions are accurately satisfied in the simulations. When these precautions are taken, there is excellent agreement between analysis and simulations, to within 10 %, even when the stratification parameter is as low as 0.707, the Reynolds number is as low as 100 and the aspect ratio (length/diameter) of the cylinder is as low as 2, and the secondary flow velocity is as high as 0.2 times the maximum base flow velocity. The predictions of the generalized models are also significantly better than those of the original Onsager

† Email address for correspondence: kumaran@chemeng.iisc.ernet.in

https://doi.org/10.1017/jfm.2011.289 Published online by Cambridge University Press

and Carrier–Maslen models, which are restricted to thin boundary layers in the limit of high stratification parameter.

Key words: gas dynamics, rarefied gas flow

1. Introduction

Radioactive isotopes of many metals, including zinc, cadmium, iridium, selenium, tellurium, germanium and molybdenum, are used in medical and industrial applications. In medical applications, radio-isotopes are used both for diagnostics such as gallium scans for locations of inflammation and infection, indium for leukocyte imaging and molybdenum/technetium scans for high bone growth, as well as for therapy including cancer therapy using isotopes of iodine and iridium. An important industrial application is the separation of uranium isotopes for nuclear power generation. Other important applications include non-destructive testing using gamma cameras, and use of zinc isotopes to reduce corrosion in reactor cooling systems.

Centrifugal separation in a high-speed rotating flow is a widely used method for isotope separation. This is because isotopes are chemically identical, and cannot be separated by chemical means. The small difference in the molecular masses of the isotopes provides the only economically feasible method for effecting separation. The centrifugal force results in a small difference in concentration of the two isotopes, with a higher concentration of the heavier isotope near the wall of the cylinder, and a higher concentration of the lighter isotope near the axis. In order to separate the two isotopes, stationary tubes and baffles are inserted into the rotating cylinder. The inserts, as well as temperature gradients along the rotating cylindrical surface and the temperature difference between the end caps, cause a secondary flow in the cylinder, which could be as important for the separation process as the concentration difference in the base solid-body rotation. For this reason, it is important to analyse the secondary flow in a high-speed cylinder.

The Onsager model was developed for calculating the secondary flows generated by applied forces in a rotating fluid in a cylinder. The secondary flow velocities are small compared to the velocity of the base flow, which is a solid-body rotation about the cylinder axis. Linearization is used for the secondary flow, where the equations of motion are truncated to linear order in the velocity and pressure disturbances to the base flow. Additional assumptions in the Onsager model include high aspect ratio (length of the cylinder is large compared to the diameter), constant temperature in the base state (isothermal condition), high Reynolds number Re and high stratification parameter $\mathscr{A}$, where the Reynolds number $Re = (\rho_w \Omega R^2/\mu)$, the stratification parameter $\mathscr{A} = \sqrt{m\Omega^2 R^2/(2k_B T)}$, R is the cylinder radius, ρ_w is the gas density at the wall, μ is the gas viscosity (which is independent of density for rarefied gases at constant temperature), Ω is the angular velocity, T is the absolute temperature and k_B is the Boltzmann constant. (The analysis is often carried out in terms of the inverse of the Reynolds number, which is referred to as the Ekman number, but here we choose to express the results in terms of the Reynolds number for notational simplicity.) In this limit, the gas flow is restricted to a boundary layer of thickness $Re^{-1/3}R$ at the wall of the cylinder. The flow at the end caps is also restricted to a thin

https://doi.org/10.1017/jfm.2011.289 Published online by Cambridge University Press

boundary layer of thickness $Re^{-1/2}R$ in the axial coordinate, and analytical solutions for the end-cap flow were first derived by Carrier and Maslen (Olander 1981).

The present analysis of rarefied gas flow in a rotating cylinder has two objectives. The first is to remove the restriction of high stratification parameter, and to generalize the solutions to low rotation speeds where the stratification parameter may be $O(1)$. Secondly, we would like to compare the predictions with molecular simulations based on the direct simulation Monte Carlo (DSMC) method for rarefied gas flows, in order to quantify the errors resulting from the approximations at different aspect ratios and Reynolds number and stratification parameter. In this study, we have obtained analytical and numerical solutions for the secondary flows generated at the cylinder's curved surface and at the end caps due to linear wall temperature gradient and external gas inflow and outflow at the axis of the cylinder. The effect of sources of mass, momentum and energy within the flow domain are analysed. These studies show that the generalized Onsager model (for the radial boundary layer at the cylinder wall) and the generalized Carrier–Maslen model (for the axial boundary layer at the end caps) are in agreement with numerical solutions to within 10 % for stratification parameter as low as 0.707, Reynolds number as low as 100 and for cylinders with length/diameter ratio as low as 2, provided the wall-slip in both the flow velocity and temperature are incorporated in the analytical solutions.

A differential equation for the 'master potential' for the secondary flow in a rotating cylinder was first presented in an unpublished report by Onsager in 1965 (Wood & Morton 1980). This equation was a sixth-order differential equation in the radial coordinate, and was valid for high rotational velocities where the gas density decreases exponentially from the wall of the cylinder due to the centrifugal force (the ideal gas equation is used to relate the pressure to the density). The model, which has subsequently been referred to as the 'Onsager pancake model' predicts that the flow is restricted to a thin boundary layer at the wall of thickness $Re^{-1/3}R$ smaller than the cylinder radius. The flow at the end caps of the cylinder was analysed by Carrier and Maslen in 1962 (Olander 1981), who derived a fourth-order differential equation for the axial variation of the streamfunction at the end caps. This model predicts that the flow is restricted to a boundary layer of thickness $Re^{-1/2}R$ at the end caps.

The basic derivation of the Onsager model was presented by Wood & Morton (1980), and the formulation of the boundary conditions was also discussed. The equations for the master potential were derived in a very general form and include the effects of sources of mass, momentum and energy. It was shown that the complete solution for the flow in the radial boundary layer can be obtained as the sum of three types of fundamental solutions, the zero eigenvalue mode for which the axial eigenvalues are zero and there is no variation in the axial direction, the end-driven mode where the eigenvalues are real and there is an exponential decay from the end caps, and the lateral modes where the eigenvalues are imaginary and the solutions decay sinusoidally in the axial direction. The solutions for the Ekman boundary layer at the end caps were also presented, with some numerical results. The Onsager model equations derived by Wood & Morton (1980) have been approximately solved by a variety of techniques, such as eigenfunction-expansion methods (Wood & Morton 1980), finite difference methods (Viecelli 1983), and finite element methods (Gunzburger & Wood 1982; Gunzburger, Wood & Jordan 1984).

The main assumptions taken into account in deriving the Onsager equation are that the configuration is axisymmetric and the flow field is a small perturbation about an isothermal solid-body rotation. The rotational speed of the cylinder is high enough that the bulk of the fluid is present in the 'Stewartson layer' of thickness $Re^{-1/3}R$ smaller

https://doi.org/10.1017/jfm.2011.289 Published online by Cambridge University Press

than the cylinder radius at the outer wall. This assumption enables us to linearize the equations of viscous compressible flow, neglect terms that are small in the limit of high Reynolds number and stratification parameter, and obtain a sixth-order equation in the radial direction for the 'master potential', which is related to the density, velocity and temperature fields. The curvature of the outer surface is usually neglected since the boundary layer thickness is small compared to the cylinder radius, but Wood, Jordan & Gunzburger (1984) also included the effect of curvature of the outer wall of the cylinder, to obtain the Onsager–Maslen equation.

Gunzburger & Wood (1982) used the finite element methods for the approximate solution of the Onsager equation. Two numerical examples were presented to show the viability of these methods, one for flow driven by a linear temperature gradient along the sidewall of the cylinder, and other for flow driven by axial mass fluxes through the end caps of the cylinder. Wood & Sanders (1983) carried out numerical studies of the Onsager pancake model for rotating compressible fluid in a cylinder with internal sources or sinks of mass, momentum or energy. Some sample calculations were presented to illustrate the counter-current flow produced by sources of mass, the three components of momentum, and energy.

Gunzburger *et al.* (1984) considered the finite element method for the approximate solution of flow in a rapidly rotating gas cylinder. The model equations to be discretized are derived based on the Onsager pancake approximation. Various analytical and computational features of the finite element method have been discussed, and a series of illustrative numerical examples is given. An alternative derivation of the equations in terms of the 'temperature potential' (instead of the Onsager master potential) was presented by Bourn, Peterson & Wood (1999), who also discussed the boundary conditions and the eigenfunction solutions of the resulting boundary value problem. A finite element solution procedure was described, and the results of the calculations have been compared with the eigenfunction solutions to the Onsager pancake equation (Wood & Morton 1980). Babarsky, Herbst & Wood (2002) introduced the properties of the temperature potential and its relationship to the original problem of axisymmetric flow in a rapidly rotating cylinder based on the Onsager master potential, and provide a firm mathematical foundation for the solutions of these two problems. They have shown that the temperature potential plays a role analogous to that of the Onsager master potential, and the Onsager minimum entropy principle for axisymmetric flow was derived in order to place the discussion of temperature potential in context. The governing equations and accompanying boundary conditions have been derived, and the relationship of these new eigensolutions to the original Onsager eigensolution is explained in terms of super-symmetry. The authors state that one of the advantages of the temperature-potential method is that it makes it easier to study the non-axisymmetric flows, since the non-axisymmetric temperature operator can be constructed by considering it to be a small perturbation of the self-adjoint operator associated with the axisymmetric temperature potential.

Although the Onsager pancake model was originally developed to study the steady, axisymmetric flows in a rapidly rotating cylinder, it was later applied to non-axisymmetric flows. Matsuda & Nakagawa (1983) studied the flow in a pie-shaped cylinder of infinite length with walls at fixed angles in the meridional direction, and reported the presence of a 'buoyancy' boundary layer of thickness $Re^{-1/2}$ times the cylinder radius at the walls perpendicular to the meridional direction. Wood & Babarsky (1992) and Babarsky & Wood (1990) extended the work of Matsuda & Nakagawa (1983) to a finite-length, pie-shaped cylinder about the vertex. They presented an eigenfunction expansion based on the spectral decomposition of

https://doi.org/10.1017/jfm.2011.289 Published online by Cambridge University Press

the resulting differential operator. However, it must be noted that studies of non-axisymmetric flows in a rotating cylinder using the boundary layer technique are still relatively rare, and the modification of the Onsager model to incorporate non-axisymmetric effects is still a challenge.

The secondary flows generated inside a high-speed rotating cylinder have been studied by numerical solutions of the compressible Navier–Stokes equations by many authors in the two-dimensional axisymmetric (r–z) configuration, the polar (r–θ) configuration and the three-dimensional (r–θ–z) configuration. These equations are solved, subject to boundary conditions, to determine the density, velocity and temperature fields. Nakayama & Torii (1974) analysed the Stewartson layers by assuming that the height is larger than the thickness of the $Re^{-1/4}R$ and $Re^{-1/3}R$ layers, by expanding the equations in terms of the ratio of thickness to the height. Bark & Bark (1976) determined the exact solution for the $Re^{-1/4}R$ layer and asymptotic solutions for the $Re^{-1/3}R$ layer, as well as numerical solutions, assuming that the cylinder walls are thermally conducting, and the wall temperature is a constant. The work of Matsuda (1976) was one of the first to stress the importance of the thermal boundary condition on the flow field, particularly if the walls are thermally insulated. The combined effect of the compressibility of the fluid and the thermal insulation of the walls produces a flow very distinct from that of Boussinesq fluids, and from that of compressible fluids confined in a cylinder with thermally conducting walls. Matsuda & Hashimoto (1978) divided the flow field in the r–z plane into several regions: the inner inviscid core, the Stewartson $Re^{-1/4}R$ layer along the sidewall, its extension to the top and bottom Ekman layers with thickness $Re^{-1/2}R$, the Stewartson $Re^{-1/3}R$ layer and its extension to the Ekman layers. In a frame rotating with the angular velocity Ω there is no flow in the inner core on account of the Taylor–Proudman theorem. Along the sidewall, however, there must be an azimuthal flow in order to satisfy the side-wall conditions. This azimuthal flow does not satisfy the boundary conditions at the top and bottom end plates, leading to the formation of the top and bottom Ekman layers with thickness $Re^{-1/2}R$, which in turn induce a meridional flow of order $Re^{-1/2}R$ in the $Re^{-1/4}R$ layer owing to Ekman suction. This flow then circulates through the $Re^{-1/3}R$ layer and in the Ekman extensions.

Brouwers (1978) studied the axisymmetric steady flow of a perfect gas in a rotating cylinder by applying a linearized analysis to a small perturbation about isothermal rigid-body rotation. Special attention was focused on the effect of the length-to-radius ratio, and on the effect of a strong radial density gradient associated with the isothermal rigid-body rotation. From the analysis, it appears that the flow outside the Ekman boundary layers consists of three types, corresponding to $1 \ll L_* \ll Re^{1/2}$, $Re^{1/2} \sim L_* \ll Re$ and $Re \sim L_*$, where L_* is the ratio of the cylinder length and the radial boundary layer thickness. For $1 \ll L_* \ll Re^{1/2}$, there is an inviscid flow near the cylinder wall, because radial diffusion is not confined to the Stewartson boundary layers but extends to the core. For $L_* \sim Re^{1/2}$ and $L_* \sim Re$, the Stewartson layers become of the same thickness as the density boundary layer. At the same time, the corresponding layers in the core go to the wall and join; as a result, for $L_* \geqslant Re$, radial diffusion is significant in the entire cylinder.

Three-dimensional Navier–Stokes simulations of flows affected by an inserted stationary object, modelled as a stationary disk extended in the meridional direction, has been performed by Volosciuk (1981) and Walz, Volosciuk & Schutz (1983). Numerical investigations have also been made of thermally, mechanically and thermo-mechanically driven flows of a weakly compressible gas in a cylinder assuming an axisymmetric continuum flow (Harada 1980*a*). The finite difference method was

https://doi.org/10.1017/jfm.2011.289 Published online by Cambridge University Press

developed for these computations based on the Euler upwind scheme. It was found that an almost-cylindrical Couette flow was established in an annulus, despite the end effects of the plates which generate mechanically driven circulations. The two mechanically driven circulations interact with the thermally driven circulations. The authors also investigated the axisymmetric continuum flow of a strongly compressible rotating gas driven thermally and mechanically in an annulus using the finite difference method. The DuFort–Frankel upwind scheme was used for efficient computations of the strongly compressible rotating flows, and it was found that the thermally driven flow becomes weaker as the compressibility is increased. The viscous dissipation increases the gas temperature of the mechanically driven flow despite cooling by the expansion work.

Sakurai (1981) analysed the axisymmetric steady centrifugally driven thermal convection of a compressible fluid in a rapidly rotating circular motion. He clarified the importance of the effect of the flow-induced volume change of a fluid particle, and proposed a method of solution. The effect of inserted objects was analysed in terms of linearized thin-wing theory by Sakurai (1981). The analysis showed that the drag force on one inserted object was not affected by other upstream objects, or by the wake of the same object due to fluid circulation, though the objects do interact with respect to their effect on the flow.

Two-dimensional continuum simulations have also been carried out in the r–θ plane for the rotating flow past a fixed object. Here, one of the objectives is to analyse the high-speed shock wave that forms when a rotating flow encounters a stationary object. Hittinger, Holt & Soubbaramayer (1981) and Hittinger *et al.* (1983) obtained a bow shock in front of a stationary object in their simulations. Two-dimensional numerical simulation of flow past a stationary object has been done by Mikami (1981, 1985), and three-dimensional inlet flows have been simulated by Aoki & Suzuki (1985). In the simulations, they assumed a uniform upstream flow, and were able to resolve the shock waves that result. The centrifugally driven thermal convection near the cooled rotor cover of a cylinder was studied by Mikami (1973). In this analysis, the boundary layer equations are reduced to ordinary differential equations by the Lees–Levy transformation, and solved numerically by applying the quasi-linearization method. Sample solutions for radial and azimuthal velocity profiles are presented. Kai (1983) studied the drag on the gas due to a stationary cylindrical object, and then equated it with a viscous drag due to an axisymmetric equivalent disk. A modified version of the Newton method was adopted to get the full solution in static state for nonlinear equations.

Jung (1983) obtained an analytical solution of the linearized flow equations using the method of eigenvalues. Starting from the rigid rotation, a linear set of partial differential equations was derived by applying the perturbation method in a strongly rotating cylinder filled with an ideal gas. In this analysis, the interior of the cylinder was divided into the bulk flow and the Ekman boundary layer near the end caps. For the bulk flow in the cylinder, dimensionless equations were formulated, and reduced by a separation method to get a set of ordinary differential equations with an arbitrary parameter. The Frobenius method was applied to get an analytical solution. The fundamental system was represented as a power series, where the relevant coefficients were calculated recursively. To solve the boundary value problem, derivatives of the fundamental system were found, which are related to the axial and tangential velocity and to the temperature deviation. In the case of Ekman layers, the Prandtl simplifications were used to get a fourth-order ordinary differential equation,

https://doi.org/10.1017/jfm.2011.289 Published online by Cambridge University Press

which was then integrated analytically. The above two types of solutions are then superimposed to solve the axisymmetric boundary value problem for the cylinder.

A finite difference algorithm for computing the secondary flow field in a rotating cylinder was described by Ribando (1984). The linearized axisymmetric Navier–Stokes equations in primitive variable form are solved by a time-marching technique. Most previous finite difference solution algorithms for rotating flows have involved numerically resolving the thin Ekman layers at the ends using an extremely fine mesh. In contrast, Ribando (1984) applied an analytical matching condition at the ends which has the same effect on the flow outside the Ekman layers as the direct application of the hydrodynamic and thermal boundary conditions.

Axially linear inner and outer temperature distributions and velocity slip were investigated by Berger (1987). An existence condition for a class of non-trivial, one-dimensional solutions was given. Exact solutions were derived using the finite gap approximation with velocity slip. The usual one-dimensional, axially symmetric solution was obtained as a limiting case. Analysis of compressible, finite length, circular Couette flow was also reported in Berger (1987). The thermal and hydrodynamical analysis of a counter-current gas flow in a rotating cylinder was carried out by Andrade & Bastos (1998). In this work, the importance of the thermal boundary conditions was demonstrated. A structural thermal model of the rotating flow was considered and analysis was carried out with realistic thermal boundary conditions.

To summarize, there are two broad classes of theoretical approaches to high-speed rotating flows in a cylinder. The first is based on the Onsager and Carrier–Maslen models, where the linearization approximation is used to derive equations for the master potential and the velocity potential, which are then solved analytically. The second is based on the linearization of the compressible Navier–Stokes equations. The latter is more exact, in the sense that there are fewer approximations made in deriving the final equations, and also because shock-type solutions can be obtained in the plane perpendicular to the axis of rotation. However, continuum equations are unsuited to flows such as that in a high-speed rotating cylinder, where there is large variation in the Knudsen number, and the mean free path is comparable to the macroscopic scale in some regions. It is necessary to specify boundary conditions at an artificial boundary where there is transition from the continuum to the free-molecular regime.

The Onsager and Carrier–Maslen equations have the advantage that analytical solutions can be obtained using the eigenfunction expansion procedure, resulting in a simpler formulation with better physical understanding. Moreover, the structure of the analytical solution ensures that there is no need to specify artificial boundary conditions, and the continuum equations for the master potential can be solved all the way to the centre of the cylinder. Of course, there is the question of whether the continuum equations accurately reproduce the flow dynamics in the region where the Knudsen number is not small. This leads to the second part of our study, where we compare the results of the Onsager and Carrier–Maslen models with molecular simulations based on the DSMC technique.

Here, we formulate a generalization of the Onsager and Carrier–Maslen equations where the restriction on high stratification parameter is removed. This involves retaining terms in the equation for the master potential which were neglected due to the high stratification parameter assumptions, while still neglecting terms due to the assumption of high (length/radius) ratio and high Reynolds number. First, we show how the equation for the master potential is obtained from the linearized Navier–Stokes equations, and evaluate the magnitudes of all the terms. This order-

https://doi.org/10.1017/jfm.2011.289 Published online by Cambridge University Press

of-magnitude analysis is used to justify the simplification to the generalized Onsager equation for the axial flow at the curved surface of the cylinder, and the generalized Carrier–Maslen model for the flow along the end caps. This serves to clarify the approximations involved in deriving the Onsager and Carrier–Maslen equations.

The resulting sixth-order operator for the master potential in the generalized Onsager model, and the fourth-order operator for the velocity potential in the generalized Carrier–Maslen model, are still self-adjoint, and therefore the eigenvalues of this operator are real, the eigenfunctions are orthogonal, and they form a complete function space. However, the eigenvalues and the eigenfunctions are now dependent on the stratification parameter, and are evaluated either by a Frobenius expansion or by numerical integration. These are then used to obtain solutions for the secondary axial flow and radial end-cap flow due to a temperature gradient along the curved surface of the cylinder, and where it is due to gas feed along the axis. We also examine the secondary flows due to mass, momentum and energy inputs/outputs within the flow domain, by solving the inhomogeneous generalized Onsager equation using the method of separation of variables.

The analytical results are compared with molecular simulations using the direct simulation Monte Carlo (DSMC) method (Bird 1963, 1994). Many previous studies have obtained velocity profiles in rotating flows using the compressible Navier–Stokes equations. However, there are currently no molecular simulation studies of high-speed rotating flows in literature, though there have been studies of high-speed stratified flows past objects (Hausman & Roberts 1984; Roberts 1985; Roberts & Hausman 1988). The present work provides an opportunity for validating both the generalized Onsager model and the DSMC method for high-speed rotating flows.

The molecular simulation procedure is more computationally intensive than the continuum Navier–Stokes equations, but it also has two important advantages. The Navier–Stokes equations are written for the macroscopic density and velocity fields, and these are applicable only when the mean free path in the gas is small compared to the macroscopic scale (radius of the cylinder or boundary layer thickness). There are many situations in high-speed rotating flows where the gas density in the central region of the cylinder is sufficiently small that the mean free path is comparable to the cylinder radius. In these cases, the Navier–Stokes equations are not valid near the centre, and it is necessary to specify artificial ‘boundary conditions’ at a surface within the flow. In this context, Roblin & Doneddu (2000) performed DSMC simulations to study the feed gas expansion from the central pipe, and the residual gas contained in the casing in which the cylinder rotates. These simulations were used to provide more realistic boundary conditions for continuum fluid flow calculations. In the second case, DSMC simulations were used to determine the mechanical power of the rotating cylinder and the heat flux dissipated on the rotating cylinder and the fixed cylinder of the casing. The possible dependence of the solutions on these artificial boundary conditions poses difficulties in the interpretation of results. No such difficulties exist in the molecular simulations, since it is only necessary to specify particle–wall interaction parameters.

Another advantage of molecular simulations is that the velocity slip at the wall resulting from the particle–wall interaction law can be obtained directly from the simulations, whereas the slip velocity has to be modelled in the continuum numerical solutions. In the present simulations, we also find that there is substantial ‘temperature slip’ in the DSMC simulations, that is, the gas temperature at the wall is not equal to the wall temperature. Both velocity and temperature slip at the walls are measured in the DSMC simulations, and these are then incorporated into the analytical solutions, in

https://doi.org/10.1017/jfm.2011.289 Published online by Cambridge University Press

order to make a quantitative comparison of the results of the analysis and simulations. The comparisons are carried out for relatively large secondary flows, where the scaled temperature gradient (for thermally driven flow) or the scaled secondary flow rate (for flows due to input/output of gas in the cylinder) is as large as 0.2, and where the aspect ratio (ratio of length to diameter of cylinder) is as small as 2. In addition, we consider stratification parameters as low as 0.707 and Reynolds numbers as low as 100, in order to quantitatively estimate the accuracy of the Onsager model.

There are technical intricacies in the implementation of sources of mass, momentum and energy within the flow in the DSMC simulations. In order to mimic a Dirac delta function in the simulations, mass, momentum and energy are inserted/removed over a small source domain of radius 10^{-3} times the cylinder radius at the designated location. When quantitative comparison has to be made with analytical solutions for specified rates of input/output of mass, momentum and energy, care has to be taken in the simulations due to the coupling between mass, momentum and energy sources. When molecules are added in simulations, there is the simultaneous addition of the momentum and energy of these molecules. In order to add mass alone, it is necessary to reduce the momentum and energy of all molecules in the source domain so that total momentum and energy are conserved. In a similar manner, momentum is added by increasing the mean velocity of the molecules in the source domain, while addition of energy requires increasing the fluctuating velocity of the molecules while keeping the total mean velocity constant. Another complication is that addition of energy at a location near the wall in the simulation causes an increase in the local fluctuating velocities of molecules, which heats up the wall. This violates the constant temperature boundary condition that is used in the analytical solution, and so it is necessary to extract heat locally at the wall in the simulation to ensure that the wall temperature is kept constant.

In § 2, the linearized mass, momentum and energy conservation equations for an axisymmetric flow in a cylindrical coordinate system are presented and different dimensionless numbers are defined. The equations for perturbations to the base state (solid-body rotation) are then used to get the equation for the master potential in § 3. In § 4, the radial boundary layer equations are solved to obtain the generalized Onsager equation, while the equation for the streamfunction for the axial boundary layer is used to obtain the generalized Carrier–Maslen equation for the axial boundary layer in § 5. In § 6, a brief summary on molecular simulation based on DSMC method is presented. In § 7, secondary flow due to linear wall temperature gradient and inflow/outflow of gas along the axis is studied and analytical results are compared with those of DSMC simulations. In § 8, secondary flow due to internal sources is analysed and analytical results are compared with those of DSMC simulations. The important conclusions of the analysis are summarized in § 9.

2. Formulation

The configuration consists of a right circular cylinder of radius R and height Z rotating at a constant angular velocity Ω. A cylindrical coordinate system with origin at the bottom of the cylinder along the axis of rotation, with radial, meridional and axial coordinates r, θ, and z respectively, is used. Throughout this analysis, we assume that the flow is axisymmetric, so there is no dependence on the meridional coordinate θ. Gravitational acceleration is neglected, since it has a negligible effect on high-speed gas flows. The compressible mass, momentum and energy conservation equations in the cylindrical coordinate system are provided in the Appendix for

https://doi.org/10.1017/jfm.2011.289 Published online by Cambridge University Press

reference. There are six variables in these equations: the density ρ, the three components of the velocity v_r, v_θ, v_z, the pressure p and the temperature T. In (A 1)–(A 5), $\mathscr{S}_m$ is the mass source density (mass input per unit volume per unit time), f_r, f_θ and f_z are the force densities in the r, θ and z directions respectively, and $\mathscr{S}_e$ is the energy source density (energy input per unit volume per unit time).

The pressure is related to the density by the ideal gas equation of state,

$$\rho = \frac{pm}{k_B T}, \tag{2.1}$$

where m is the mass of a molecule and k_B is the Boltzmann constant.

If the temperature on the walls of the cylinder is uniform, and there is no inflow or outflow of gas, a steady solution for the equations of motion is one where the gas undergoes solid-body rotation with angular velocity Ω at constant temperature. The temperature $\bar{T}$ and the components of the velocity $\bar{\boldsymbol{v}}$ in the base state in this steady state are

$$\bar{v}_\theta = \Omega r, \quad \bar{v}_z = 0, \quad \bar{v}_r = 0, \quad \bar{T} = T_0, \tag{2.2}$$

where T_0 is the constant temperature. The pressure is obtained by solving the radial momentum equation,

$$\frac{\mathrm{d}\bar{p}}{\mathrm{d}r} = \bar{\rho}\Omega^2 r = \frac{\bar{p}m\Omega^2 r}{k_B T_0}, \tag{2.3}$$

where $\bar{\rho}$ is the density at steady state, together with the ideal gas equation of state,

$$\bar{\rho} = \frac{\bar{p}m}{k_B T_0}, \tag{2.4}$$

where m is the mass of a molecule and k_B is the Boltzmann constant. The above equation is easily solved to obtain

$$\frac{\bar{p}}{\bar{p}_w} = \frac{\bar{\rho}}{\bar{\rho}_w} = \exp\left(-\mathscr{A}^2\left(1 - \frac{r^2}{R^2}\right)\right), \tag{2.5}$$

where $\bar{p}_w$ and $\bar{\rho}_w$ are the pressure and density at the wall in the unperturbed state, and $\mathscr{A}$ is the stratification parameter defined below. The total mass of gas in the cylinder is related to ρ_w by

$$\text{Mass of gas} = \frac{2\pi R^2 Z\bar{\rho}_w(1 - \exp(-\mathscr{A}^2))}{2\mathscr{A}^2}, \tag{2.6}$$

where Z is the total height of the cylinder.

It is useful to discuss the different dimensionless numbers used in the analysis. The stratification parameter obtained from the equation for the density is

$$\mathscr{A} = \sqrt{\frac{m\Omega^2 R^2}{2k_B T_0}} \propto \frac{R\Omega}{c_s}, \tag{2.7}$$

where $R\Omega$ is the characteristic flow velocity, and $c_s = \sqrt{\gamma k_B T_0/m}$ is the speed of sound. The Reynolds number, used a little later, is defined by

$$Re = \frac{\rho_w \Omega R^2}{\bar{\mu}}, \tag{2.8}$$

https://doi.org/10.1017/jfm.2011.289 Published online by Cambridge University Press

where $\bar{\mu}$ is the viscosity of the fluid in the unperturbed state. The viscosity of a dilute gas scales as

$$\bar{\mu} \sim \frac{\sqrt{mk_BT_0}}{d^2}, \tag{2.9}$$

where m is the molecular mass and d is the molecular diameter. Using the above expression for the viscosity, it can easily be verified that the Reynolds number can be rewritten as

$$Re \sim \frac{\mathscr{A}}{Kn}, \tag{2.10}$$

where the Knudsen number is defined by

$$Kn = (m/\sqrt{2}\pi\rho_w d^2 R) = (\lambda/R), \tag{2.11}$$

where $\lambda = (m/\sqrt{2}\pi\rho_w d^2)$ is the mean free path at the wall. The other dimensionless groups used are the Prandtl number and the ratio of specific heats,

$$Pr = \frac{C_p\bar{\mu}}{\bar{K}}, \tag{2.12}$$

$$\gamma = \frac{C_p}{C_v}, \tag{2.13}$$

which are both $O(1)$ for an ideal gas.

3. Equations of motion in axisymmetric coordinates

The disturbance to the base state due to a temperature gradient at the walls, or due to a small mass flux through the cylinder, is incorporated by perturbing the base velocity and pressure profile as follows:

$$\rho = \bar{\rho} + \tilde{\rho}, \tag{3.1}$$

$$p = \bar{p} + \tilde{p}, \tag{3.2}$$

$$T = \bar{T} + \tilde{T}, \tag{3.3}$$

$$v_r = \tilde{v}_r, \tag{3.4}$$

$$v_\theta = r\Omega + \tilde{v}_\theta, \tag{3.5}$$

$$v_z = \tilde{v}_z. \tag{3.6}$$

The above forms for the dynamical variables are inserted into the mass, momentum and energy conservation equations, and linearized in the perturbation (tilde) quantities. Steady state is assumed, so that all the time derivatives are zero. After subtracting the corresponding base-state equations, we obtain the following equations for the perturbations:

$$\frac{1}{r}\frac{\partial}{\partial r}(r\bar{\rho}\tilde{v}_r) + \frac{\partial}{\partial z}(\bar{\rho}\tilde{v}_z) = \mathscr{S}_m, \tag{3.7}$$

$$\begin{aligned} -\tilde{\rho}\Omega^2 r - 2\bar{\rho}\Omega\tilde{v}_\theta \;&=\; -\frac{\partial\tilde{p}}{\partial r} + \bar{\mu}\left(\frac{\partial}{\partial r}\left(\frac{1}{r}\frac{\partial}{\partial r}(r\tilde{v}_r)\right) + \frac{\partial^2\tilde{v}_r}{\partial z^2}\right) \\ &\quad + \left(f_r + \frac{\bar{\mu}}{3}\frac{\partial\mathscr{S}_m}{\partial r}\right), \end{aligned} \tag{3.8}$$

$$2\bar{\rho}\Omega\tilde{v}_r = \bar{\mu}\left(\frac{\partial}{\partial r}\left(\frac{1}{r}\frac{\partial}{\partial r}(r\tilde{v}_\theta)\right) + \frac{\partial^2\tilde{v}_\theta}{\partial z^2}\right) + f_\theta, \tag{3.9}$$

https://doi.org/10.1017/jfm.2011.289 Published online by Cambridge University Press

$$0 = -\frac{\partial \tilde{p}}{\partial z} + \bar{\mu}\left(\frac{1}{r}\frac{\partial}{\partial r}\left(r\frac{\partial \tilde{v}_z}{\partial r}\right) + \frac{\partial^2 \tilde{v}_z}{\partial z^2}\right) + \left(f_z + \frac{\bar{\mu}}{3}\frac{\partial \mathscr{S}_m}{\partial z}\right), \tag{3.10}$$

$$-\bar{\rho}\Omega^2 r\tilde{v}_r = -\bar{p}\mathscr{S}_m + \bar{K}\left(\frac{1}{r}\frac{\partial}{\partial r}\left(r\frac{\partial \tilde{T}}{\partial r}\right) + \frac{\partial^2 \tilde{T}}{\partial z^2}\right) + \mathscr{S}_e. \tag{3.11}$$

Here, $\bar{\mu}$ and $\bar{K}$ are the viscosity and thermal conductivity of the gas in the base state, where the temperature is T_0. Note that in the ideal gas limit, the viscosity and thermal conductivity are functions of the temperature alone, and they do not depend on the density. In (3.8), the term on the left is the contribution to the r momentum equation due to the centrifugal force, while in (3.9), the left side represents the contribution to the θ momentum equation due to the Coriolis force. In the energy equation (3.11), the term on the left is the pressure work done due to the compression or expansion of the gas, and we have used the equation of state (2.4) and the mass conservation equation (3.7) to simplify this term. The perturbation to the equation of state is

$$\tilde{\rho} = \left(\frac{m}{k_B T_0}\right)\tilde{p} - \bar{\rho}\left(\frac{\tilde{T}}{T_0}\right). \tag{3.12}$$

First, we eliminate the density in the r momentum equation, (3.8), using the equation of state, (3.12), to obtain

$$\begin{aligned} &-\frac{\Omega^2 rm\tilde{p}}{k_B T_0} + \frac{\Omega^2 r\bar{\rho}\tilde{T}}{T_0} - 2\bar{\rho}\Omega\tilde{v}_\theta + \frac{\partial \tilde{p}}{\partial r} \\ &\quad = \bar{\mu}\left(\frac{\partial}{\partial r}\left(\frac{1}{r}\frac{\partial}{\partial r}(r\tilde{v}_r)\right) + \frac{\partial^2 \tilde{v}_r}{\partial z^2}\right) + \left(f_r + \frac{\bar{\mu}}{3}\frac{\partial \mathscr{S}_m}{\partial r}\right). \end{aligned} \tag{3.13}$$

The identity,

$$\begin{aligned} \bar{\rho}\frac{\partial}{\partial r}\left(\frac{\tilde{p}}{\bar{\rho}}\right) &= \frac{\partial \tilde{p}}{\partial r} - \frac{\tilde{p}}{\bar{\rho}}\frac{\partial \bar{\rho}}{\partial r} \\ &= \frac{\partial \tilde{p}}{\partial r} - \frac{\tilde{p}m\Omega^2 r}{k_B T_0}, \end{aligned} \tag{3.14}$$

can be inserted into the momentum conservation equation, (3.13), to obtain

$$\begin{aligned} &\frac{1}{r}\frac{\partial}{\partial r}\left(\frac{\tilde{p}}{\bar{\rho}}\right) - \frac{2\Omega\tilde{v}_\theta}{r} - \frac{\Omega^2\tilde{T}}{T_0} \\ &\quad = \frac{\bar{\mu}}{\bar{\rho}r}\left(\frac{\partial}{\partial r}\left(\frac{1}{r}\frac{\partial}{\partial r}(r\tilde{v}_r)\right) + \frac{\partial^2 \tilde{v}_r}{\partial z^2}\right) + \frac{1}{\bar{\rho}r}\left(f_r + \frac{\bar{\mu}}{3}\frac{\partial \mathscr{S}_m}{\partial r}\right). \end{aligned} \tag{3.15}$$

If we take the derivative of the above equation with respect to the z coordinate, we obtain

$$\begin{aligned} &\frac{1}{r}\frac{\partial}{\partial r}\left(\frac{1}{\bar{\rho}}\frac{\partial \tilde{p}}{\partial z}\right) - \Omega\frac{\mathrm{d}}{\mathrm{d}z}\left(\frac{2\tilde{v}_\theta}{r} - \frac{\Omega\tilde{T}}{T_0}\right) \\ &\quad = \frac{\bar{\mu}}{\bar{\rho}r}\frac{\partial}{\partial z}\left(\frac{\partial}{\partial r}\left(\frac{1}{r}\frac{\partial}{\partial r}(r\tilde{v}_r)\right) + \frac{\partial^3 \tilde{v}_r}{\partial z^3}\right) + \frac{1}{\bar{\rho}r}\frac{\partial}{\partial z}\left(f_r + \frac{\bar{\mu}}{3}\frac{\partial \mathscr{S}_m}{\partial r}\right). \end{aligned} \tag{3.16}$$

https://doi.org/10.1017/jfm.2011.289 Published online by Cambridge University Press

Equation (3.10) is used to substitute for $(\partial\tilde{p}/\partial z)$ in the above equation, to obtain

$$\left(\frac{1}{r}\frac{\partial}{\partial r}\left(\frac{1}{\bar{\rho}r}\frac{\partial}{\partial r}\left(r\frac{\partial\tilde{v}_z}{\partial r}\right)+\frac{1}{\bar{\rho}}\frac{\partial^2\tilde{v}_z}{\partial z^2}\right)\right)$$
$$-\frac{\partial}{\partial z}\left(\frac{1}{\bar{\rho}r}\frac{\partial}{\partial r}\left(\frac{1}{r}\frac{\partial(r\tilde{v}_r)}{\partial r}\right)+\frac{1}{\bar{\rho}r}\frac{\partial^3\tilde{v}_r}{\partial z^3}\right)-\frac{\Omega}{\bar{\mu}}\frac{\mathrm{d}}{\mathrm{d}z}\left(\frac{2\tilde{v}_\theta}{r}-\frac{\Omega\tilde{T}}{T_0}\right)$$
$$=\frac{1}{\bar{\mu}\bar{\rho}r}\frac{\partial}{\partial z}\left(f_r+\frac{\bar{\mu}}{3}\frac{\partial\mathscr{S}_m}{\partial r}\right)-\frac{1}{\bar{\mu}r}\frac{\partial}{\partial r}\left(\frac{1}{\bar{\rho}}\left(f_z+\frac{\bar{\mu}}{3}\frac{\partial\mathscr{S}_m}{\partial z}\right)\right). \tag{3.17}$$

Here, the viscosity $\bar{\mu}$ in the base state is independent of position, because the temperature is uniform and the viscosity depends only on temperature.

The velocity components $\tilde{v}_r$ and $\tilde{v}_z$ can be expressed in terms of a streamfunction using the mass conservation equation (3.7),

$$r\bar{\rho}\tilde{v}_r=-\frac{\partial\psi}{\partial z}+\int_{r_0}^{r}\mathscr{S}_m r\,\mathrm{d}r, \tag{3.18}$$

$$r\bar{\rho}\tilde{v}_z=\frac{\partial\psi}{\partial r}, \tag{3.19}$$

where the difference in the streamfunction between two radial locations gives the axial mass flux in the region between these two locations,

$$\psi(a,z)-\psi(r,z)=\int_{r}^{a}\bar{\rho}\tilde{v}_z r\,\mathrm{d}r. \tag{3.20}$$

Expressed in terms of the streamfunction, (3.17) is

$$\frac{1}{r}\frac{\partial}{\partial r}\left(\frac{1}{\bar{\rho}r}\frac{\partial}{\partial r}\left(r\frac{\partial}{\partial r}\right)+\frac{1}{\bar{\rho}}\frac{\partial^2}{\partial z^2}\right)\left(\frac{1}{\bar{\rho}r}\frac{\partial\psi}{\partial r}\right)+\left(\frac{1}{\bar{\rho}r}\frac{\partial}{\partial r}\left(\frac{1}{r}\frac{\partial}{\partial r}\left(r\frac{\partial}{\partial z}\right)\right)+\frac{1}{\bar{\rho}r}\frac{\partial^3}{\partial z^3}\right)$$
$$\times\left(\frac{1}{\bar{\rho}r}\left(\frac{\partial\psi}{\partial z}-\int_{r_0}^{r}\mathscr{S}_m r\,\mathrm{d}r\right)\right)-\frac{\Omega}{\bar{\mu}}\frac{\partial}{\partial z}\left(\frac{2\tilde{v}_\theta}{r}-\frac{\Omega\tilde{T}}{T_0}\right)$$
$$=\frac{1}{\bar{\mu}\bar{\rho}r}\frac{\partial}{\partial z}\left(f_r+\frac{\bar{\mu}}{3}\frac{\partial\mathscr{S}_m}{\partial r}\right)-\frac{1}{\bar{\mu}r}\frac{\partial}{\partial r}\left(\frac{1}{\bar{\rho}}\left(f_z+\frac{\bar{\mu}}{3}\frac{\partial\mathscr{S}_m}{\partial z}\right)\right). \tag{3.21}$$

The streamfunction ψ is expressed in terms of the 'master potential' χ:

$$\psi=\frac{1}{r}\frac{\partial\chi}{\partial r}. \tag{3.22}$$

This is inserted into the momentum conservation equation (3.17), to obtain

$$\frac{1}{r}\frac{\partial}{\partial r}\left(\frac{1}{\bar{\rho}r}\frac{\partial}{\partial r}\left(r\frac{\partial}{\partial r}\right)+\frac{1}{\bar{\rho}}\frac{\partial^2}{\partial z^2}\right)\left(\frac{1}{\bar{\rho}r}\frac{\partial}{\partial r}\left(\frac{1}{r}\frac{\partial\chi}{\partial r}\right)\right)$$
$$+\left(\frac{1}{\bar{\rho}r}\frac{\partial}{\partial r}\left(\frac{1}{r}\frac{\partial}{\partial r}\left(r\frac{\partial}{\partial z}\right)\right)+\frac{1}{\bar{\rho}r}\frac{\partial^3}{\partial z^3}\right)$$
$$\times\left(\frac{1}{\bar{\rho}r^2}\frac{\partial}{\partial r}\left(\frac{\partial\chi}{\partial z}\right)-\frac{1}{\bar{\rho}r}\int_{r_0}^{r}\mathscr{S}_m r\,\mathrm{d}r\right)-\Omega\frac{\partial}{\partial z}\left(\frac{2\tilde{v}_\theta}{r}-\frac{\Omega\tilde{T}}{T_0}\right)$$
$$=\frac{1}{\bar{\mu}\bar{\rho}r}\frac{\partial}{\partial z}\left(f_r+\frac{\bar{\mu}}{3}\frac{\partial\mathscr{S}_m}{\partial r}\right)-\frac{1}{\bar{\mu}r}\frac{\partial}{\partial r}\left(\frac{1}{\bar{\rho}}\left(f_z+\frac{\bar{\mu}}{3}\frac{\partial\mathscr{S}_m}{\partial z}\right)\right). \tag{3.23}$$

https://doi.org/10.1017/jfm.2011.289 Published online by Cambridge University Press

4. Axial flow

Further development of the equation for the master potential depends on whether the boundary layer considered is in the radial or the axial direction. When the boundary layer is in the radial coordinate, the radial derivatives of $\tilde{v}_\theta$ and $\tilde{T}$ on the right sides of (3.9) and (3.11) are balanced by the left sides. The angular velocity $\tilde{v}_\theta$ in (3.23) can be expressed in terms of the master potential as follows. The angular momentum conservation equation (3.9) can be rewritten as

$$2\bar{\rho}\Omega\tilde{v}_r = \bar{\mu}\left(\frac{1}{r^2}\frac{\partial}{\partial r}\left(r^3\frac{\partial}{\partial r}\left(\frac{\tilde{v}_\theta}{r}\right)\right) + \frac{\partial^2\tilde{v}_\theta}{\partial z^2}\right) + f_\theta. \tag{4.1}$$

In this equation, the velocity $\tilde{v}_r$ is expressed in terms of the master potential using (3.18) and (3.22):

$$\begin{aligned}&\frac{\partial}{\partial z}\left(\frac{-2\Omega}{r^2}\frac{\partial\chi}{\partial r}\right) + \frac{2\Omega}{r}\int_{r_0}^{r}\mathscr{S}_m r\,\mathrm{d}r \\ &\quad = \bar{\mu}\left(\frac{1}{r^2}\frac{\partial}{\partial r}\left(r^3\frac{\partial}{\partial r}\left(\frac{\tilde{v}_\theta}{r}\right)\right) + \frac{\partial^2\tilde{v}_\theta}{\partial z^2}\right) + f_\theta.\end{aligned} \tag{4.2}$$

The above equation is multiplied throughout by r^2, and integrated once with respect to the radial coordinate, to obtain

$$\begin{aligned}&-2\Omega\frac{\partial\chi}{\partial z} + 2\Omega\left.\frac{\partial\chi}{\partial z}\right|_{r=r_0} + 2\Omega\int_{r_0}^{r} r\left[\int_{r_0}^{r}\mathscr{S}_m r\,\mathrm{d}r\right]\mathrm{d}r \\ &\quad = \bar{\mu}\left(\left.r^3\frac{\partial}{\partial r}\left(\frac{\tilde{v}_\theta}{r}\right)\right|_{r} - \left.r^3\frac{\partial}{\partial r}\left(\frac{\tilde{v}_\theta}{r}\right)\right|_{r=r_0}\right) \\ &\qquad + \bar{\mu}\int_{r_0}^{r} r^2\,\mathrm{d}r\left(\frac{\partial^2\tilde{v}_\theta}{\partial z^2}\right) + \int_{r_0}^{r} f_\theta r^2\,\mathrm{d}r.\end{aligned} \tag{4.3}$$

Here r_0 is a reference location which will be discussed a little later. Equation (4.3) is differentiated with respect to the z coordinate, and multiplied by $(2\Omega/\bar{\mu}^2 r^4)$, to obtain

$$\begin{aligned}&\frac{4\Omega^2}{\bar{\mu}^2 r^4}\frac{\partial^2\chi}{\partial z^2} - \frac{4\Omega^2}{\bar{\mu}^2 r^4}\int_{r_0}^{r} r\left[\int_{r_0}^{r}\frac{\partial\mathscr{S}_m}{\partial z} r\,\mathrm{d}r\right]\mathrm{d}r + R_\theta \\ &\quad = -\frac{2\Omega}{\mu}\frac{\partial}{\partial z}\left(\frac{1}{r}\frac{\partial}{\partial r}\left(\frac{\tilde{v}_\theta}{r}\right)\right) + C_\theta + \frac{2\Omega}{\bar{\mu}^2 r^4}\frac{\partial}{\partial z}\left(\int_{r_0}^{r} f_\theta r^2\,\mathrm{d}r\right),\end{aligned} \tag{4.4}$$

where

$$R_\theta = \frac{2\Omega}{\bar{\mu} r^4}\int_{r_0}^{r} r^2\,\mathrm{d}r\left(\frac{\partial^2\tilde{v}_\theta}{\partial z^2}\right), \tag{4.5}$$

and the function C_θ, which appears as a boundary term in (4.3), is

$$C_\theta = \frac{2\Omega}{\bar{\mu} r^4}\frac{\partial}{\partial z}\left(r^3\frac{\partial}{\partial r}\left(\frac{\tilde{v}_\theta}{r}\right)\right)\Bigg|_{r=r_0} - \frac{4\Omega^2}{\bar{\mu}^2 r^4}\left(\frac{\partial^2\chi}{\partial z^2}\right)_{r=r_0}. \tag{4.6}$$

https://doi.org/10.1017/jfm.2011.289 Published online by Cambridge University Press

The temperature perturbation $\tilde{T}$ in (3.23) can be expressed in terms of the master potential from the energy equation, (3.11). Expressing the radial velocity $\tilde{v}_r$ in terms of the master potential using (3.18) and (3.22), we obtain

$$\frac{\Omega^2}{r}\frac{\partial}{\partial r}\left(\frac{\partial \chi}{\partial z}\right) - \Omega^2 \int_{r_0}^{r} \mathscr{S}_m r \,\mathrm{d}r = -\bar{p}\mathscr{S}_m + \bar{K}\left(\frac{1}{r}\frac{\partial}{\partial r}\left(r\frac{\partial \tilde{T}}{\partial r}\right) + \frac{\partial^2 \tilde{T}}{\partial z^2}\right) + \mathscr{S}_e. \quad (4.7)$$

The above equation can be multiplied by r, integrated once with respect to the radial coordinate with lower limit r_0 and upper limit r, to obtain

$$\begin{aligned}\Omega^2\left(\frac{\partial \chi}{\partial z}\right) - \Omega^2 \int_{r_0}^{r} r\left[\int_{r_0}^{r} \mathscr{S}_m r \,\mathrm{d}r\right]\mathrm{d}r \\ = \bar{K}\left(r\frac{\partial \tilde{T}}{\partial r}\right)\bigg|_{r} - \bar{K} r \frac{\partial \tilde{T}}{\partial r}\bigg|_{r=r_0} + \int_{r_0}^{r} r\,\mathrm{d}r\left(\frac{\partial^2 \tilde{T}}{\partial z^2}\right) + \int_{r_0}^{r} (\mathscr{S}_e - \bar{p}\mathscr{S}_m) r \,\mathrm{d}r. \quad (4.8)\end{aligned}$$

This is then multiplied by $(\Omega^2/\bar{K}T_0 r^2)$, and differentiated once with respect to z, to obtain

$$\begin{aligned}\frac{\Omega^4}{\bar{K}\bar{\mu}T_0 r^2}\frac{\partial^2 \chi}{\partial z^2} - \frac{\Omega^4}{\bar{K}\bar{\mu}T_0 r^2}\int_{r_0}^{r} r\left[\int_{r_0}^{r} \frac{\partial \mathscr{S}_m}{\partial z} r \,\mathrm{d}r\right]\mathrm{d}r + R_T + C_T \\ = \frac{\Omega^2}{\bar{\mu}}\frac{1}{r}\frac{\partial}{\partial r}\frac{\partial}{\partial z}\left(\frac{\tilde{T}}{T_0}\right) + \frac{\Omega^2}{\bar{K}\bar{\mu}T_0 r^2}\left(\frac{\partial}{\partial z}\int_{r_0}^{r} (\mathscr{S}_e - \bar{p}\mathscr{S}_m) r \,\mathrm{d}r\right), \quad (4.9)\end{aligned}$$

where

$$R_T = \frac{\Omega^2}{\bar{K}\bar{\mu}T_0 r^2}\int_{r_0}^{r} r\,\mathrm{d}r\left(\frac{\partial^3 \tilde{T}}{\partial z^3}\right), \quad (4.10)$$

and the term appearing due to the constant of integration in (4.8) is

$$C_T = \frac{\Omega^2}{T_0 r^2}\frac{\partial}{\partial z}\left(r\frac{\partial \tilde{T}}{\partial r}\bigg|_{r=r_0}\right) - \frac{\Omega^4}{\bar{K}\bar{\mu}T_0 r^2}\left(\frac{\partial^2 \chi}{\partial z^2}\right)_{r=r_0}, \quad (4.11)$$

where r_0 is a reference location to be discussed a little later.

We take the derivative $(1/r)(\partial/\partial r)$ of the equation for the master potential, (3.23), and then insert (4.4) and (4.9), to obtain

$$\begin{aligned}&\frac{1}{r}\frac{\partial}{\partial r}\left(\frac{1}{r}\frac{\partial}{\partial r}\left(\frac{1}{\bar{\rho}r}\frac{\partial}{\partial r}\left(r\frac{\partial}{\partial r}\right) + \frac{1}{\bar{\rho}}\frac{\partial^2}{\partial z^2}\right)\left(\frac{1}{\bar{\rho}r}\frac{\partial}{\partial r}\left(\frac{1}{r}\frac{\partial \chi}{\partial r}\right)\right)\right) \\ &\quad + \frac{1}{r}\frac{\partial}{\partial r}\left(\frac{1}{\bar{\rho}r}\frac{\partial}{\partial r}\left(\frac{1}{r}\frac{\partial}{\partial r}\left(r\frac{\partial}{\partial z}\right)\right) + \frac{1}{\bar{\rho}r}\frac{\partial^3}{\partial z^3}\right) \\ &\quad \times\left(\frac{1}{\bar{\rho}r^2}\frac{\partial}{\partial r}\left(\frac{\partial \chi}{\partial z}\right) - \frac{1}{\bar{\rho}r}\int_{r_0}^{r} \mathscr{S}_m r \,\mathrm{d}r\right) \\ &\quad + \left(\frac{\Omega^4}{\bar{K}\bar{\mu}T_0 r^2} + \frac{4\Omega^2}{\bar{\mu}^2 r^4}\right)\frac{\partial^2 \chi}{\partial z^2} + (R_\theta + R_T) + (C_\theta + C_T) \\ &\quad = \frac{1}{r}\frac{\partial}{\partial r}\left(\frac{1}{\bar{\mu}\bar{\rho}r}\frac{\partial}{\partial z}\left(f_r + \frac{\bar{\mu}}{3}\frac{\partial \mathscr{S}_m}{\partial r}\right) - \frac{1}{\bar{\mu}r}\frac{\partial}{\partial r}\left(\frac{1}{\bar{\rho}}\left(f_z + \frac{\bar{\mu}}{3}\frac{\partial \mathscr{S}_m}{\partial z}\right)\right)\right)\end{aligned}$$

https://doi.org/10.1017/jfm.2011.289 Published online by Cambridge University Press

$$+\frac{2\Omega}{\bar{\mu}^2 r^4}\frac{\partial}{\partial z}\left(\int_{r_0}^{r} f_\theta r^2\,\mathrm{d}r\right)-\frac{\Omega^2}{\bar{K}\bar{\mu}T_0 r^2}\frac{\partial}{\partial z}\int_{r_0}^{r}(\mathscr{S}_e-\bar{p}\mathscr{S}_m)r\,\mathrm{d}r$$
$$+\left(\frac{\Omega^4}{\bar{K}\bar{\mu}T_0 r^2}+\frac{4\Omega^2}{\bar{\mu}^2 r^4}\right)\int_{r_0}^{r} r\left[\int_{r_0}^{r}\frac{\partial\mathscr{S}_m}{\partial z}r\,\mathrm{d}r\right]\mathrm{d}r. \tag{4.12}$$

The radial coordinate is expressed in terms of the scaled radial coordinate ξ, defined by

$$\xi=\mathscr{A}^2\left(1-\frac{r^2}{R^2}\right). \tag{4.13}$$

With this transformation, it can easily be verified that

$$\frac{1}{r}\frac{\partial}{\partial r}=-\frac{2\mathscr{A}^2}{R^2}\frac{\partial}{\partial\xi}, \tag{4.14}$$

where $\delta=R/(\sqrt{2}\mathscr{A})$ is the boundary layer thickness in the radial coordinate. When the equation for the master potential is expressed in terms of this scaled coordinate, and the base density profile

$$\bar{\rho}=\rho_w\exp(-\xi) \tag{4.15}$$

is used, we obtain

$$\frac{64\mathscr{A}^{12}}{\rho_w^2R^{10}}\frac{\partial}{\partial\xi^2}\left(\mathrm{e}^{\xi}\frac{\partial}{\partial\xi}\left(\left(1-\frac{\xi}{\mathscr{A}^2}\right)\frac{\partial}{\partial\xi}\left(\mathrm{e}^{\xi}\frac{\partial^2\chi}{\partial\xi^2}\right)\right)\right)+\frac{16\mathscr{A}^8}{\rho_w^2R^8}\frac{\partial^2}{\partial\xi^2}\left(\mathrm{e}^{2\xi}\frac{\partial^2}{\partial\xi^2}\frac{\partial^2\chi}{\partial z^2}\right)$$
$$+\frac{16\mathscr{A}^8}{\rho_w^2R^8}\frac{\partial}{\partial\xi}\left(\mathrm{e}^{\xi}\frac{\partial^2}{\partial\xi^2}\left(\mathrm{e}^{\xi}\frac{\partial}{\partial\xi}\frac{\partial^2\chi}{\partial z^2}\right)\right)+\frac{4\mathscr{A}^4}{\rho_w^2R^6}\frac{\partial}{\partial\xi}\left(\frac{\mathrm{e}^{2\xi}}{(1-(\xi/\mathscr{A}^2))}\frac{\partial}{\partial\xi}\frac{\partial^4\chi}{\partial z^4}\right)$$
$$+\left(\frac{\Omega^4}{\bar{K}\bar{\mu}T_0R^2(1-\xi/\mathscr{A}^2)}+\frac{4\Omega^2}{\bar{\mu}^2R^4(1-\xi/\mathscr{A}^2)^2}\right)\frac{\partial^2\chi}{\partial z^2}$$
$$+(R_\theta+R_T)+(C_\theta+C_T)=S, \tag{4.16}$$

where S represents the source term in the equation for the master potential obtained from the mass, momentum and energy sources.

The above equation can be reduced to dimensionless form by dividing by the prefactor of the first term on the left, and defining a scaled master potential. The scaling for the master potential, χ, is best inferred by balancing the first term on the left and the term on the right in (4.2), which provides $\chi^*=\chi/\bar{\mu}R^2Z$. Using this scaled master potential, we obtain

$$\frac{\partial^2}{\partial\xi^2}\left(\mathrm{e}^{\xi}\frac{\partial}{\partial\xi}\left(\left(1-\frac{\xi}{\mathscr{A}^2}\right)\frac{\partial}{\partial\xi}\left(\mathrm{e}^{\xi}\frac{\partial^2\chi^*}{\partial\xi^2}\right)\right)\right)+\frac{1}{4\mathscr{A}^4}\frac{R^2}{Z^2}\frac{\partial^2}{\partial\xi^2}\left(\mathrm{e}^{2\xi}\frac{\partial^2}{\partial\xi^2}\frac{\partial^2\chi^*}{\partial\eta^2}\right)$$
$$+\frac{1}{4\mathscr{A}^4}\frac{R^2}{Z^2}\frac{\partial}{\partial\xi}\left(\mathrm{e}^{\xi}\frac{\partial^2}{\partial\xi^2}\left(\mathrm{e}^{\xi}\frac{\partial}{\partial\xi}\frac{\partial^2\chi^*}{\partial\eta^2}\right)\right)$$
$$+\frac{1}{16\mathscr{A}^8}\frac{R^4}{Z^4}\frac{\partial}{\partial\xi}\left(\frac{\mathrm{e}^{2\xi}}{(1-(\xi/\mathscr{A}^2))}\frac{\partial}{\partial\xi}\frac{\partial^4\chi^*}{\partial\eta^4}\right)$$
$$+\left(\frac{2Re^2\mathscr{A}^2Pr(1-\gamma^{-1})}{(1-\xi/\mathscr{A}^2)}+\frac{4Re^2}{(1-\xi/\mathscr{A}^2)^2}\right)\frac{1}{64\mathscr{A}^{12}}\frac{R^2}{Z^2}\frac{\partial^2\chi^*}{\partial\eta^2}$$
$$+(R_\theta^*+R_T^*)+(C_\theta^*+C_T^*)=S^*, \tag{4.17}$$

where the Reynolds number, stratification parameter and the Prandtl number are given in (2.8), (2.7) and (2.12) respectively, and

https://doi.org/10.1017/jfm.2011.289 Published online by Cambridge University Press

$$R^*_\theta = \frac{1}{64\mathscr{A}^{14}}\frac{R^4}{Z^4}\left((1-\xi/\mathscr{A}^2)^{-2}\int_{\xi_0}^{\xi} \mathrm{d}\xi (1-\xi/\mathscr{A}^2)^{1/2}\left(\frac{\partial^3 \tilde{v}^*_\theta}{\partial \eta^3}\right)\right), \tag{4.18}$$

$$C^*_\theta = \frac{1}{16\mathscr{A}^{10}}\frac{R^2}{Z^2}\left((1-\xi/\mathscr{A}^2)^{-2}\left(\frac{\partial \tilde{v}^*_\theta}{\partial \xi}\bigg|_{\xi=\xi_0}\right)\right), \tag{4.19}$$

$$R^*_{\tilde{T}} = -\frac{1}{128\mathscr{A}^{14}}\frac{R^4}{Z^4}\left((1-\xi/\mathscr{A}^2)^{-1}\int_{\xi_0}^{\xi} \mathrm{d}\xi \left(\frac{\partial^3 \tilde{T}^*}{\partial \eta^3}\right)\right), \tag{4.20}$$

$$C^*_{\tilde{T}} = -\frac{1}{32\mathscr{A}^{10}}\frac{R^2}{Z^2}\left((1-\xi/\mathscr{A}^2)^{-1}\frac{\partial}{\partial \eta}\frac{\partial \tilde{T}^*}{\partial \xi}\bigg|_{\xi=\xi_0}\right), \tag{4.21}$$

where $\tilde{v}^*_\theta = \tilde{v}_\theta/(\Omega R)$ and $\tilde{T}^* = \tilde{T}/T_0$ and S^* is the scaled source term.

The above equation for the master potential, (4.17), can be used to assess the approximations made in the Onsager equation for the master potential which, in the present notation, is

$$\frac{\partial^2}{\partial \xi^2}\left(\mathrm{e}^{\xi}\frac{\partial}{\partial \xi}\left(\frac{\partial}{\partial \xi}\left(\mathrm{e}^{\xi}\frac{\partial^2 \chi^*}{\partial \xi^2}\right)\right)\right) + (2Re^2\mathscr{A}^2 Pr(1-\gamma^{-1}) + 4Re^2)\frac{1}{64\mathscr{A}^{12}}\frac{R^2}{Z^2}\frac{\partial^2 \chi^*}{\partial \eta^2} = \mathscr{S}^*, \tag{4.22}$$

where

$$\begin{aligned}
\mathscr{S}^*(\xi,\eta) = {} & \frac{Re}{32\mathscr{A}^{10}}\frac{R}{Z}\frac{R^2}{\mathscr{A}^4\bar{K}T_0}(1-\xi/\mathscr{A}^2)^{-1}\int_{\xi_0}^{\xi}\frac{\partial(\mathscr{S}_e - p_w\mathrm{e}^{-\xi}\mathscr{S}_m)}{\partial \eta}\mathrm{d}\xi^* \\
& - \frac{Re}{16\mathscr{A}^{10}}\frac{R}{Z}\frac{R}{\mathscr{A}^4\Omega\bar{\mu}}(1-\xi/\mathscr{A}^2)^{-2}\int_{\xi_0}^{\xi}\frac{\partial f_\theta}{\partial \eta}\left(1-\frac{\xi^*}{\mathscr{A}^2}\right)^{1/2}\mathrm{d}\xi^* \\
& - \left(\frac{2Re^2\mathscr{A}^2 Pr(1-\gamma^{-1})}{(1-\xi/\mathscr{A}^2)} + \frac{4Re^2}{(1-\xi/\mathscr{A}^2)^2}\right)\frac{1}{256\mathscr{A}^{16}} \\
& \times \frac{R}{\rho_w\Omega Z}\int_{\xi_0}^{\xi}\left[\int_{\xi_0}^{\xi^*}\frac{\partial \mathscr{S}_m(\xi^{**},\eta)}{\partial \eta}\mathrm{d}\xi^{**}\right]\mathrm{d}\xi^* \\
& + \frac{R^4}{16\mathscr{A}^8 Z^2\bar{\mu}}\left(\frac{\partial}{\partial \xi}\left(\mathrm{e}^{\xi}\frac{\partial}{\partial \xi}\left(\frac{\partial}{\partial \xi}\left(\left(1-\frac{\xi}{\mathscr{A}^2}\right)^{1/2}\frac{\partial}{\partial \eta}\right)\right)\right)\right. \\
& \left. + \frac{R^2}{Z^2}\frac{\partial}{\partial \xi}\left(\frac{\mathrm{e}^{\xi}}{(1-\xi/\mathscr{A}^2)^{1/2}}\frac{\partial^3}{\partial \eta^3}\right)\right)\left[\frac{\mathrm{e}^{\xi}}{(1-\xi/\mathscr{A}^2)^{1/2}}\int_{\xi_0}^{\xi}\mathscr{S}_m\,\mathrm{d}\xi^*\right] \\
& - \frac{Re}{32\mathscr{A}^{10}}\left[\frac{1}{\rho_w\Omega^2 Z}\frac{\partial}{\partial \xi}\left(\frac{1}{(1-\xi/\mathscr{A}^2)^{1/2}}\right.\right. \\
& \left.\times\frac{\partial}{\partial \eta}\left(\mathrm{e}^{\xi}\left(f_r - \frac{2\bar{\mu}}{3}\frac{A^2}{R}\left(1-\frac{\xi}{A^2}\right)^{1/2}\frac{\partial \mathscr{S}_m}{\partial \xi}\right)\right)\right) \\
& \left. + \frac{1}{\rho_w\Omega^2 R}\frac{\partial^2}{\partial \xi^2}\left(\mathrm{e}^{\xi}\left(f_z + \frac{\bar{\mu}}{3Z}\frac{\partial \mathscr{S}_m}{\partial \eta}\right)\right)\right].
\end{aligned} \tag{4.23}$$

https://doi.org/10.1017/jfm.2011.289 Published online by Cambridge University Press

In the above equation, the contribution to S^* due to the fourth term on the right side of the above equation (fourth and fifth lines of (4.23)) is $O(Re^{-1}(R/Z))$ smaller than that due to the third term on the right side (third line in (4.23)). Therefore, this can be neglected in the leading approximation. The magnitude of the other terms do depend on the source strengths, and so these cannot be neglected in general. However, (4.23) provides the conditions under which the source strengths are significant, that is, for $\mathscr{S}_m \sim (\rho_w \Omega Z/R)$, $f_r \sim (\rho_w \Omega^2 R/Re)$, $f_\theta \sim (\Omega \bar{\mu} Z/R^2 Re)$, $f_z \sim (\rho_w \Omega^2 R/Re)$ and $S_e \sim (\bar{K} T_0 Z/R^3 Re)$.

The following terms in (4.17) are neglected in the Onsager equation (4.22).

(*a*) The second, third and fourth terms on the left side of (4.17) are neglected, because the parameter $(R^2/Z^2\mathscr{A}^4) \ll 1$. Clearly, this is valid for high-aspect-ratio cylinders, $Z \gg R$, and also when the stratification parameter is large.

(*b*) The sixth term on the left is also neglected in comparison to the fifth term on the left side. It can easily be verified, from (4.1) and (4.7), that these terms are also $O(R^2/\mathscr{A}^4 Z^2)$ smaller than the fifth term on the left side of (4.17).

(*c*) The seventh term on the left side of (4.17) is also neglected. The value of this term depends on the location of the boundary surface $\xi = \xi_0$. In the present case, this boundary is at the centre of the cylinder. Symmetry requires that the angular velocity (v_θ/r) $(\partial(v_\theta/r)/\partial r) = 0$, and $(\partial T/\partial r) = 0$. Therefore, C_T and C_θ are identically zero in this case. However, for the flow in the annulus between two cylinders rotating at different velocities, these terms are not necessarily zero.

(*d*) Within the first term on the left of (4.17), a term proportional to $(\xi/\mathscr{A}^2)$ is neglected. Similarly, within the fifth term on the left, it is assumed that $(1+\xi/\mathscr{A}^2) \approx 1$. These imply that the stratification parameter $\mathscr{A} \gg 1$.

(*e*) The first and fifth terms on the left side of (4.17) are retained in the Onsager equation (4.22), implying that either $(Re^2/16\mathscr{A}^{12})(R^2/Z^2) \sim 1$, or $(Re^2 Pr(1-\gamma^{-1})/32\mathscr{A}^{10})(R^2/Z^2) \sim 1$.

The limitation $\mathscr{A} \gg 1$ imposed by condition (*d*) above can be relaxed if we formulate a generalized Onsager equation,

$$L_6^{\mathscr{A}}(\chi^*) + \frac{Re^2}{64\mathscr{A}^{12}} \frac{R^2}{Z^2} \frac{\partial^2 \chi^*}{\partial \eta^2} = S^*, \tag{4.24}$$

where the scaled source term S^* was defined in (4.23), and the linear differential operator $L_6^{\mathscr{A}}$ in the ξ coordinate is defined by

$$L_6^{\mathscr{A}} = \left(\frac{2\mathscr{A}^2 Pr(1-\gamma^{-1})}{(1-\xi/\mathscr{A}^2)} + \frac{4}{(1-\xi/\mathscr{A}^2)^2} \right)^{-1} \times \left(\frac{\partial^2}{\partial \xi^2} \left(e^{\xi} \frac{\partial}{\partial \xi} \left(\left(1 - \frac{\xi}{\mathscr{A}^2} \right) \frac{\partial}{\partial \xi} \left(e^{\xi} \frac{\partial^2}{\partial \xi^2} \right) \right) \right) \right). \tag{4.25}$$

The operator has been written with the superscript $^{\mathscr{A}}$ to indicate that there is an explicit dependence on the stratification parameter. This operator also depends on the Prandtl number Pr and the ratio of specific heats, but these are gas properties and not flow properties, and are both $O(1)$ for an ideal gas. Therefore, the only flow dependence in the operator $L_6^{\mathscr{A}}$ enters through the stratification parameter, while the Prandtl number and ideal gas constant are determined by the nature of the gas. Here, we will assume an ideal gas of hard spheres, for which $Pr = 0.95$ and $\gamma = 1.066$.

https://doi.org/10.1017/jfm.2011.289 Published online by Cambridge University Press

It is easily verified that this operator is also self-adjoint, when the inner product is defined by

$$(A_1, B_1) = \int_0^{\xi_0} \mathrm{d}\xi\, w(\xi) A_1(\xi) B_1(\xi), \tag{4.26}$$

where the weight function $w(\xi)$ is given by

$$w(\xi) = \left(\frac{2\mathscr{A}^2 Pr(1-\gamma^{-1})}{(1-\xi/\mathscr{A}^2)} + \frac{4}{(1-\xi/\mathscr{A}^2)^2} \right), \tag{4.27}$$

and the boundary conditions are appropriately specified, as discussed next. Therefore, the eigenvalues of this operator are real, and the eigenfunctions are orthogonal. We refer to (4.24) as the 'generalized' Onsager equation, to distinguish this from the Onsager equation (4.22). Since (4.17) is a sixth-order differential equation, it is necessary to specify three boundary conditions at each boundary. Here we will consider the homogeneous form of the Onsager and generalized Onsager equations and we will investigate the secondary flow due to wall thermal forcing and external inflow/outflow of gas into the rotating cylinder. For the flow in a cylinder where $r_0 = 0$, the boundary conditions at the centre are as follows. The following expressions for the velocity components and the axial flow rate are useful for specifying the boundary conditions:

$$\tilde{v}_r = \frac{2R\Omega\mathscr{A}^2}{Re} \left(1 - \frac{\xi}{\mathscr{A}^2}\right)^{-1/2} \mathrm{e}^{\xi} \frac{\partial^2 \chi^*}{\partial\xi\,\partial\eta}, \tag{4.28}$$

$$\tilde{v}_z = \frac{4Z\Omega\mathscr{A}^4}{Re} \mathrm{e}^{\xi} \frac{\partial^2 \chi^*}{\partial\xi^2}, \tag{4.29}$$

$$\begin{aligned} F_z &= 2\pi \int_0^R r\,\mathrm{d}r \bar{\rho} \tilde{v}_z \\ &= \frac{4\pi\rho_w R^2 \Omega Z \mathscr{A}^2}{Re} \frac{\partial \chi^*}{\partial\xi}\bigg|_0^{\xi}, \end{aligned} \tag{4.30}$$

where F_z is the total flow rate in the axial direction. Since the velocity potential is related only to derivatives of the master potential χ, adding a constant to χ does not change the velocity fields. Therefore, without loss of generality, we can impose at the centre

$$\chi^* = 0. \tag{4.31}$$

The zero radial velocity boundary condition at the centre requires that $(\partial\psi/\partial z) = 0$, or

$$\frac{\partial \chi^*}{\partial\xi} = 0. \tag{4.32}$$

Symmetry requires that the radial derivative of the axial velocity has to be zero at the centre of the cylinder. Therefore,

$$\frac{\partial \tilde{v}_z}{\partial r} = 0. \tag{4.33}$$

Now,

$$\bar{\rho}\tilde{v}_z = \frac{1}{r}\frac{\partial}{\partial r}\left(\frac{1}{r}\frac{\partial\chi}{\partial r}\right), \tag{4.34}$$

https://doi.org/10.1017/jfm.2011.289 Published online by Cambridge University Press

or

$$\bar{\rho}_w \tilde{v}_z = \left(\frac{4\mathscr{A}^4}{R^4}\right)\left(\mathrm{e}^{\xi}\frac{\partial^2\chi}{\partial\xi^2}\right). \tag{4.35}$$

Taking the derivative with respect to ξ gives

$$\bar{\rho}_w\left(\frac{\partial\tilde{v}_z}{\partial\xi}\right) = \left(\frac{4\mathscr{A}^4}{R^4}\right)\left(\frac{\partial}{\partial\xi}\left(\mathrm{e}^{\xi}\frac{\partial^2\chi}{\partial\xi^2}\right)\right). \tag{4.36}$$

From the condition that the radial derivative of the axial velocity is zero, we obtain

$$\frac{\partial}{\partial\xi}\left(\mathrm{e}^{\xi}\frac{\partial^2\chi^*}{\partial\xi^2}\right) = 0, \tag{4.37}$$

or

$$L_3^{\mathscr{A}}(\chi^*) = 0, \tag{4.38}$$

where

$$L_3^{\mathscr{A}}(\chi^*) = \left(1 - \frac{\xi}{\mathscr{A}^2}\right)\frac{\partial}{\partial\xi}\left(\mathrm{e}^{\xi}\frac{\partial^2\chi^*}{\partial\xi^2}\right). \tag{4.39}$$

At the wall $r = R(\xi = 0)$, the condition for the total axial mass flow rate (4.30) can be used to obtain a boundary condition for the master potential χ^*. Since $(\partial\chi^*/\partial\xi) = 0$ at the centre, the total flow rate condition reduces to

$$\frac{\partial\chi^*}{\partial\xi} = F^*, \tag{4.40}$$

where $F^* = FRe/(4\pi\mathscr{A}^2R^2\Omega Z\rho_w)$ is the scaled axial flow rate. The axial velocity condition at the wall can be written as

$$\frac{\partial^2\chi^*}{\partial\xi^2} = V_z^*, \tag{4.41}$$

where $V_z^* = \tilde{v}_z Re/(4\mathscr{A}^4\Omega Z)$ is the scaled axial velocity at the wall. It might be expected that the axial velocity should be zero at the wall from the no-slip condition, but in the DSMC simulations, we find that the axial velocity is not zero at the wall, and there is a slip velocity. This slip velocity V_z^* is included in the boundary condition (4.41).

The third boundary condition at the outer wall emerges from the temperature at the outer surface of the cylinder. This boundary condition is formulated from (3.23) for the master potential, in which we neglect the axial gradients of the master potential in comparison to the radial derivatives. Since the velocity perturbation $\tilde{v}_\theta$ is zero at the cylindrical surface, the boundary condition reduces to

$$\frac{1}{r}\frac{\partial}{\partial r}\left(\frac{1}{\bar{\rho}r}\frac{\partial}{\partial r}\left(r\frac{\partial}{\partial r}\right)\right)\left(\frac{1}{r}\frac{\partial}{\partial r}\left(\frac{1}{\bar{\rho}r}\frac{\partial\chi}{\partial r}\right)\right) = -\frac{\Omega^2}{\bar{\mu}T_0}\left(\frac{\partial\tilde{T}}{\partial z}\right). \tag{4.42}$$

The temperature boundary condition at the outer wall (from (4.42)) is expressed in terms of scaled coordinates as

$$L_5^{\mathscr{A}}(\chi^*) = -\frac{Re^2}{32\mathscr{A}^{10}}\frac{R^2}{Z^2}\left(\frac{1}{T_0}\frac{\partial\tilde{T}}{\partial\eta}\right), \tag{4.43}$$

https://doi.org/10.1017/jfm.2011.289 Published online by Cambridge University Press

where the operator $L_5^{\mathscr{A}}$ is

$$L_5^{\mathscr{A}} = \frac{\partial}{\partial\xi}\left(\mathrm{e}^{\xi}\frac{\partial}{\partial\xi}\left(\left(1-\frac{\xi}{\mathscr{A}^2}\right)\frac{\partial}{\partial\xi}\left(\mathrm{e}^{\xi}\frac{\partial^2}{\partial\xi^2}\right)\right)\right). \tag{4.44}$$

Note that in general, (4.43) provides the boundary condition for a linear combination of the perturbation in $\tilde{v}_\theta$ and $\tilde{T}$, and not their individual boundary conditions. Since $\tilde{v}_\theta$ is zero at the outer surface, (4.43) reduces to a boundary condition for $\tilde{T}$. Finally, we note that in the case of flow in an annular region, the equivalents of (4.31), (4.32) and (4.38) can still be used at the inner boundary provided the axial velocity is zero. However, the terms C_θ and C_T will no longer be zero.

Explicit solutions are easily obtained for the Onsager equation, in the limit $\mathscr{A} \gg 1$, when there is a temperature gradient at the wall and a net axial flow of material. The most general solution for the Onsager equation, (4.22), is

$$\begin{aligned}\chi^* = {} & (C_0\xi\mathrm{e}^{-2\xi} + C_1\mathrm{e}^{-2\xi} + C_2\xi\mathrm{e}^{-\xi} + C_3\mathrm{e}^{-\xi} + C_4\xi + C_5) \\ & + (D_0\xi\mathrm{e}^{-2\xi} + D_1\mathrm{e}^{-2\xi} + D_2\xi\mathrm{e}^{-\xi} + D_3\mathrm{e}^{-\xi} + D_4\xi + D_5)\eta.\end{aligned} \tag{4.45}$$

In the limit of large stratification parameter, boundary conditions (4.31)–(4.38) can be applied in the limit $\xi \to \infty$, resulting in the coefficients

$$C_2 = C_4 = C_5 = D_2 = D_4 = D_5 = 0. \tag{4.46}$$

The boundary conditions at the wall, (4.40)–(4.43), can now be used to determine the other coefficients:

$$C_0 + D_0\eta = -\frac{Re^2}{32\mathscr{A}^{10}}\frac{R^2}{Z^2}\frac{1}{T_0}\frac{\partial\tilde{T}}{\partial\eta}, \tag{4.47}$$

$$C_1 + D_1\eta = \frac{F^*}{2} + \frac{V_z^*}{2} - \frac{3Re^2}{256\mathscr{A}^{10}}\frac{R^2}{Z^2}\frac{1}{T_0}\frac{\partial\tilde{T}}{\partial\eta}, \tag{4.48}$$

$$C_3 + D_3\eta = -2F^* - V^* + \frac{Re^2}{64\mathscr{A}^{10}}\frac{R^2}{Z^2}\frac{1}{T_0}\frac{\partial\tilde{T}}{\partial\eta}. \tag{4.49}$$

Analytical solutions can also be obtained for the generalized Onsager equation (4.24):

$$\begin{aligned}\chi^* = {} & (C_0 + D_0\eta)(2\mathscr{A}^2(1-2\mathscr{A}^2)\mathrm{e}^{-2\xi} + 4\mathscr{A}^4(2+2\mathscr{A}^2-2\xi) \\ & \times \mathrm{Ei}(2\mathscr{A}^2-2\xi)\mathrm{e}^{-2\mathscr{A}^2} - 8\mathscr{A}^4\mathrm{e}^{-(\xi+\mathscr{A}^2)}\mathrm{Ei}(\mathscr{A}^2-\xi)) + (C_1 + D_1\eta) \\ & \times (-2\mathscr{A}^2\mathrm{e}^{-2\xi} + 2\mathscr{A}^2(2+2\mathscr{A}^2-2\xi)\mathrm{e}^{-2\mathscr{A}^2}\mathrm{Ei}(2\mathscr{A}^2-2\xi) \\ & - 4\mathscr{A}^2\mathrm{e}^{-(\xi+\mathscr{A}^2)}\mathrm{Ei}(\mathscr{A}^2-\xi)) + (C_2 + D_2\eta) \\ & \times (-4\mathscr{A}^2\mathrm{e}^{-\xi} + 2\mathscr{A}^2(2+2\mathscr{A}^2-2\xi)\mathrm{e}^{-\mathscr{A}^2}\mathrm{Ei}(\mathscr{A}^2-\xi)) \\ & + (C_3 + D_3\eta)\mathrm{e}^{-\xi} + (C_4 + D_4\eta)\xi + (C_5 + D_5\eta),\end{aligned} \tag{4.50}$$

where $\mathrm{Ei}(x)$ is the exponential integral

$$\mathrm{Ei}(x) = \int_{-\infty}^{x} \mathrm{d}t\frac{\mathrm{e}^t}{t}. \tag{4.51}$$

The coefficients in the above equation have to be determined numerically from the boundary conditions (4.31)–(4.38) at $\xi = \mathscr{A}^2$, and (4.40)–(4.43) at $\xi = 0$.

https://doi.org/10.1017/jfm.2011.289 Published online by Cambridge University Press

Next, we consider the secondary flow due to mass/momentum/energy sources within the domain, with homogeneous boundary conditions (constant temperature with no net inflow/outflow). Since (4.24) is linear in the master potential, any solution can be written as the sum of two parts, one due to secondary flow driven by wall inhomogeneities and the second due to internal sources. As shown below, the solution for the master potential with internal sources can be obtained by the separation-of-variables method, since the differential operators in both the axial and radial directions are self-adjoint. The homogeneous boundary conditions for (4.24) are as follows. At the wall ($\xi = 0$), the boundary conditions are the no-penetration condition in the radial direction, the no-slip condition in the axial and meridional direction and the zero temperature perturbation condition. The homogeneous radial and axial velocity boundary conditions, $\tilde{v}_r = 0$ and $\tilde{v}_z = 0$ at $r = R$ ($\xi = 0$), reduce to

$$\frac{\partial \chi^*}{\partial \xi} = 0, \tag{4.52}$$

$$\frac{\partial^2 \chi^*}{\partial \xi^2} = 0, \tag{4.53}$$

while a combination of the zero meridional velocity and temperature conditions is given by

$$L_5^{\mathscr{A}}(\chi^*) = 0, \tag{4.54}$$

where the operator $L_5^{\mathscr{A}}$ is given in (4.44). At the centre of the cylinder, $\xi = \xi_0 = \mathscr{A}^2$ (which corresponds to $r = 0$ along the axis of the cylinder), the symmetry conditions are zero radial velocity $\tilde{u}_r = 0$, zero axial shear stress $\partial \tilde{u}_z / \partial r = 0$, which can be written as

$$\frac{\partial \chi^*}{\partial \xi} = 0, \tag{4.55}$$

$$L_3^{\mathscr{A}}(\chi^*) = 0, \tag{4.56}$$

where the operator $L_3^{\mathscr{A}}$ is given in (4.39). In addition, since the velocity and temperature perturbations are related to the derivatives of the master potential, the master potential itself can be set equal to zero, without loss of generality, at any point along the axis of the cylinder. We choose to set the master potential equal to zero at a point along the axis. Then, from the boundary condition (4.55), the master potential is equal to zero at all points on the axis $\xi = \xi_0$, that is,

$$\chi^* = 0. \tag{4.57}$$

In the η direction, the boundary conditions are the zero normal velocity conditions at the end caps,

$$\chi^* = 0 \quad \text{at } \eta = 0, \tag{4.58}$$

$$\chi^* = 0 \quad \text{at } \eta = 1. \tag{4.59}$$

It is not possible to apply tangential velocity and heat flux conditions in the η direction, since the governing (4.24) is a second-order differential equation in η.

To obtain the solution, we use the separation-of-variables procedure. First, we define the eigenvalues and eigenfunctions of the operators $L_6^{\mathscr{A}}$ and $(\partial^2/\partial \eta^2)$. For the $L_6^{\mathscr{A}}$ operator, the eigen-relation can be written as

$$L_6^{\mathscr{A}} F_n(\xi) = \alpha_n F_n(\xi), \tag{4.60}$$

https://doi.org/10.1017/jfm.2011.289 Published online by Cambridge University Press

Eigenvalue	$\mathscr{A} = 0.707$	$\mathscr{A} = 2.121$	$\mathscr{A} = 3.535$	$\mathscr{A} = 7.071$
α_1	1.759667752	1.222999401	0.993690028	0.880107000
α_2	5.429232944	3.199011956	2.875330185	2.715002000
α_3	7.584621679	4.288809040	3.957040016	3.792706000
α_4	9.152088622	5.075719241	4.741827469	4.576442000
α_5	10.423997022	5.714588795	5.378748931	5.212398520
α_6	11.437183104	6.221185252	5.885343106	5.718991564
α_7	12.304130798	6.654661576	6.318817774	6.152465413
α_8	13.061696307	7.033446226	6.697601158	6.531248169
α_9	13.734373020	7.369786090	7.033940015	6.867586527
α_{10}	14.339260350	7.672230990	7.336384089	7.183030193

TABLE 1. First 10 eigenvalues of $L_6^{\mathscr{A}}$ operator at stratification parameters 0.707, 2.121, 3.535, 7.071.

where α_n are the discrete eigenvalues. The adjoint of the linear operator $L_6^{\mathscr{A}}$, with boundary conditions (4.52)–(4.57), can be calculated as

$$\begin{aligned}
&\int_0^{\xi_0} \mathrm{d}\xi\, w(\xi) A_1(\xi) L_6^{\mathscr{A}}(B_1(\xi)) \\
&= \left(A_1 L_5^{\mathscr{A}} B_1 - (d_\xi A_1) L_4^{\mathscr{A}} B_1 + (d_\xi^2 A_1) \left(\mathrm{e}^\xi \left(1 - \frac{\xi}{\mathscr{A}^2} \right) \right) L_3^{\mathscr{A}} B_1 \right. \\
&\quad \left. - (d_\xi^2 B_1) \left(\mathrm{e}^\xi \left(1 - \frac{\xi}{\mathscr{A}^2} \right) \right) L_3^{\mathscr{A}} A_1 + (d_\xi A_1) L_4^{\mathscr{A}} B_1 - B_1 L_5^{\mathscr{A}} A_1 \right) \Bigg|_{\xi=0}^{\xi=\xi_0} \\
&\quad + \int_0^{\xi_0} \mathrm{d}\xi\, w(\xi) B_1(\xi) L_6^{\mathscr{A}}(A_1(\xi)),
\end{aligned} \tag{4.61}$$

where

$$L_4^{\mathscr{A}} A_1 = \mathrm{e}^\xi \frac{\partial}{\partial \xi} \left(\left(1 - \frac{\xi}{\mathscr{A}^2} \right) \frac{\partial}{\partial \xi} \left(\mathrm{e}^\xi \frac{\partial^2 A_1}{\partial \xi^2} \right) \right). \tag{4.62}$$

It is clear from (4.61) that the operator $L_6^{\mathscr{A}}$, with boundary conditions (4.52)–(4.57), is a self-adjoint operator, since all the terms on the right side obtained by partial integration are zero. Therefore, the eigenvalues α_n in (4.60) are real, and the eigenfunctions $F_n(\xi)$ are orthogonal. We define the eigenfunctions so that they are orthonormal:

$$\int_0^{\xi_0} \mathrm{d}\xi\, F_n(\xi) F_m(\xi) = \delta_{mn}. \tag{4.63}$$

The eigenvalues and eigenfunctions are determined numerically using fourth-order Runge–Kutta integration and the shooting technique. The first ten eigenvalues (α_n) of the operator $L_6^{\mathscr{A}}$ at $\mathscr{A} = 0.707$, 2.121, 3.535 and 7.071 are given in table 1. The first four eigenfunctions at different stratification parameters $\mathscr{A} = 0.707$, 2.121, 3.535 are plotted in figure 1(*a*).

The eigen-equation for the η direction is

$$\frac{\partial^2 G_n(\eta)}{\partial \eta^2} = \beta_n G_n(\eta), \tag{4.64}$$

https://doi.org/10.1017/jfm.2011.289 Published online by Cambridge University Press

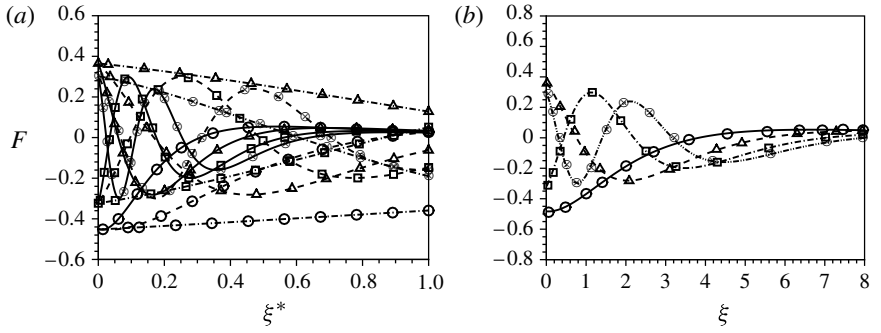


FIGURE 1. (*a*) The first four eigenfunctions at different stratification parameters as a function of ξ^*. The lines show the different stratification parameters: $\mathscr{A} = 3.535$ (—), $\mathscr{A} = 2.121$ (− −), $\mathscr{A} = 0.707$ (· − ·). The symbols show the different modes: first (○), second (Δ), third (□), fourth (⊗). (*b*) Comparison of eigenfunctions at $\mathscr{A} = 7.071$ with those of Wood & Morton (1980). The lines show the different modes: first (—), second (− −), third (· − ·), fourth (· · − · ·). The results of Wood & Morton (1980) are represented by symbols: first (○), second (Δ), third (□), fourth (⊗).

with boundary conditions (4.58) and (4.59). For this case, the eigenvalues are given by $\beta_n = (n\pi)^2$, and the orthonormal eigenfunctions are

$$G_n(\eta) = \sqrt{2}\sin(n\pi\eta). \tag{4.65}$$

The master potential can be expressed in terms of the eigenfunctions of the $L_6^{\mathscr{A}}$ and the $(\partial^2/\partial\eta^2)$ operators:

$$\chi^* = \sum_{n=1}^{\infty}\sum_{m=1}^{\infty} A_{nm}F_n(\xi)G_m(\eta). \tag{4.66}$$

The above expressions are substituted into the differential equation (4.24), and the orthogonality condition is used, to obtain the coefficients A_{mn}:

$$A_{nm} = \frac{1}{\alpha_n + ((Re/8\mathscr{A}^6)(R/Z))^2\beta_m}\int_0^{\xi_0} \mathrm{d}\xi \int_0^1 \mathrm{d}\eta S^*(\xi,\eta)F_n(\xi)G_m(\eta). \tag{4.67}$$

In the case of delta function sources,

$$\mathscr{S}^*(\xi,\eta) = \sum_{p=1}^{P} \mathscr{S}_p^*\delta(\xi-\xi_p,\eta-\eta_p), \tag{4.68}$$

the coefficients A_{nm} reduce to

$$A_{nm} = \frac{1}{\alpha_n + ((Re/8\mathscr{A}^6)(R/Z))^2\beta_m}\sum_{p=1}^{P} S_p^*F_n(\xi_p)G_m(\eta_p). \tag{4.69}$$

Here, P is the total number of sources. In the case of a complicated source expression (4.23), which involves derivatives and integrals, if the mass, momentum and energy

https://doi.org/10.1017/jfm.2011.289 Published online by Cambridge University Press

sources are of the form

$$\begin{pmatrix} \mathscr{S}_m \\ f_r \\ f_\theta \\ f_z \\ \mathscr{S}_e \end{pmatrix} = \sum_{p=1}^{P} \begin{pmatrix} \mathscr{S}_{mp} \\ f_{rp} \\ f_{\theta p} \\ f_{zp} \\ \mathscr{S}_{ep} \end{pmatrix} \delta(\xi - \xi_p)\delta(\eta - \eta_p), \tag{4.70}$$

the expression for the coefficients can be determined using integration by parts:

$$\begin{aligned}
&(\alpha_n + ((Re/8\mathscr{A}^6)(R/Z))^2\beta_m)A_{nm} \\
&= \frac{Re}{32\mathscr{A}^{10}}\frac{R}{Z}\frac{R^2(\mathscr{S}_{ep} - p_w e^{-\xi_c}S_{mp})}{4\mathscr{A}^4\bar{K}T_0}\left(-\left.\frac{\partial G_m}{\partial\eta}\right|_{\eta=\eta_c}\right)\int_{\xi_c}^{0} d\xi\,\frac{F_n(\xi)}{(1-\xi/\mathscr{A}^2)} \\
&\quad - \frac{Re}{16\mathscr{A}^{10}}\frac{R}{Z}\frac{f_{\theta p}R}{4\mathscr{A}^4\Omega\bar{\mu}}\left(-\left.\frac{\partial G_m}{\partial\eta}\right|_{\eta=\eta_c}\right)\left(1-\frac{\xi_c^*}{\mathscr{A}^2}\right)^{1/2}\int_{\xi_c}^{0} d\xi\,\frac{F_n(\xi)}{(1-\xi/\mathscr{A}^2)^2} \\
&\quad - \left(\frac{2Re^2\mathscr{A}^2Pr(1-\gamma^{-1})}{(1-\xi/\mathscr{A}^2)} + \frac{4Re^2}{(1-\xi/\mathscr{A}^2)^2}\right)\frac{\mathscr{S}_{mp}R}{256\mathscr{A}^{16}\rho_w\Omega Z} \\
&\quad \times\left(-\left.\frac{\partial G_m}{\partial\eta}\right|_{\eta=\eta_c}\right)\int_{\xi_c}^{0} d\xi F_n(\xi)(\xi-\xi_c) \\
&\quad - \frac{Re}{32\mathscr{A}^{10}}\left[\frac{\left(f_{rp} - \frac{2}{3R}\bar{\mu}\mathscr{A}^2(1-\xi_c/\mathscr{A}^2)^{1/2}\frac{\partial S_{mp}}{\partial\xi}\right)}{\rho_w\Omega^2 Z}\left(\left.\frac{\partial G_m}{\partial\eta}\right|_{\eta=\eta_c}\right)\right. \\
&\quad \times\left(\frac{e^{\xi_c}}{(1-\xi_c/\mathscr{A}^2)^{1/2}}\left.\frac{\partial F_n}{\partial\xi}\right|_{\xi=\xi_c}\right) \\
&\quad \left. + \frac{\left(f_{zp} + \frac{\bar{\mu}}{3Z}\frac{\partial S_{mp}}{\partial\eta}\right)}{\rho_w\Omega^2 R}\left(G_m(\eta_p)e^{\xi_p}\left.\frac{\partial^2 F_n(\xi)}{\partial\xi^2}\right|_{\xi=\xi_p}\right)\right].
\end{aligned} \tag{4.71}$$

Here, the fourth term on the right side of (4.23) has been neglected, since this is small compared to the third term for high Reynolds number and aspect ratio.

5. Radial flow at end caps

The discussion is restricted to radial flow at the end caps where there are no sources or sinks within the boundary layer, which turns out to be $O(Re^{-1/2})$ smaller than the cylinder radius. The analysis can easily be extended to a flow with sources and sinks, using the same methodology as that for the axial flow at the curved wall of the cylinder. For the radial flow, the axial derivatives of $\tilde{v}_\theta$ and $\tilde{T}$ on the right sides of (3.9) and (3.11) are balanced by the left sides. We start with the equation for the streamfunction, (3.21). The momentum equation in the θ direction, (4.1), is written in terms of the streamfunction,

$$-\frac{2\Omega}{r}\frac{\partial\psi}{\partial z} = \bar{\mu}\left(\frac{\partial}{\partial r}\left(\frac{1}{r}\frac{\partial}{\partial r}\left(\frac{\tilde{v}_\theta}{r}\right)\right) + \frac{\partial^2\tilde{v}_\theta}{\partial z^2}\right). \tag{5.1}$$

https://doi.org/10.1017/jfm.2011.289 Published online by Cambridge University Press

This is integrated once with respect to the z coordinate and multiplied by $-(2\Omega/\bar{\mu}^2 r)$, to obtain

$$\frac{4\Omega^2}{\bar{\mu}^2 r^2}(\psi(r,z)-\psi(r,z_0))+S_\theta+C_\theta=-\frac{2\Omega}{r}\frac{\partial\tilde{v}_\theta}{\partial z}\bigg|_{(r,z)}, \tag{5.2}$$

where z_0 is a reference location at which the boundary conditions are applied,

$$S_\theta=\int_{z_0}^{z}\mathrm{d}z\frac{2\Omega}{r}\frac{\partial}{\partial r}\left(\frac{1}{r}\frac{\partial}{\partial r}\left(\frac{\tilde{v}_\theta}{r}\right)\right), \tag{5.3}$$

and the term appearing from the constant of integration is

$$C_\theta=\frac{2\Omega}{r}\frac{\partial\tilde{v}_\theta}{\partial z}\bigg|_{r,z_0}. \tag{5.4}$$

The equation for the temperature perturbation, (4.7), can be simplified in a similar manner. When this equation is expressed in terms of the streamfunction, we obtain

$$\Omega^2\left(\frac{\partial\psi}{\partial z}\right)=\bar{K}\left(\frac{1}{r}\frac{\partial}{\partial r}\left(r\frac{\partial\tilde{T}}{\partial r}\right)+\frac{\partial^2\tilde{T}}{\partial z^2}\right). \tag{5.5}$$

This is multiplied by $\left(\Omega^2/\bar{\mu}\bar{K}T_0\right)$ and integrated once with respect to the z coordinate, to obtain

$$\frac{\Omega^4}{\bar{\mu}\bar{K}T_0}(\psi(r,z)-\psi(r,z_0))+S_T+C_T=\frac{\Omega^2}{\bar{\mu}T_0}\frac{\partial\tilde{T}}{\partial z}, \tag{5.6}$$

where

$$S_T=-\frac{\Omega^2}{\bar{\mu}T_0}\frac{1}{r}\frac{\partial}{\partial r}\left(r\frac{\partial}{\partial r}\int_{z_0}^{z}\mathrm{d}z\tilde{T}\right), \tag{5.7}$$

and the term appearing from the boundary conditions is

$$C_T=\frac{\Omega^2}{\bar{\mu}T_0}\frac{\partial\tilde{T}}{\partial z}\bigg|_{r,z_0}. \tag{5.8}$$

Equations (5.4) and (5.8) are considerably simplified if we assume that $\psi(r,z_0)$ is zero, which is valid for all flows where there is a no-slip condition at the boundary. The boundary terms C_θ and C_T depend on the boundary conditions for the stress and the heat flux, which cannot be assumed to be zero in the most general case.

Inserting (5.4) and (5.8) into (3.21) for the streamfunction, we obtain

$$\frac{1}{r}\frac{\partial}{\partial r}\left(\frac{1}{\bar{\rho}r}\frac{\partial}{\partial r}\left(r\frac{\partial}{\partial r}\right)+\frac{1}{\bar{\rho}}\frac{\partial^2}{\partial z^2}\right)\left(\frac{1}{\bar{\rho}r}\frac{\partial\psi}{\partial r}\right)+\left(\frac{1}{\bar{\rho}r}\frac{\partial}{\partial r}\left(\frac{1}{r}\frac{\partial}{\partial r}\left(r\frac{\partial}{\partial z}\right)\right)+\frac{1}{\bar{\rho}r}\frac{\partial^3}{\partial z^3}\right)$$
$$\times\left(\frac{1}{\bar{\rho}r}\left(\frac{\partial\psi}{\partial z}\right)\right)+\left(\frac{4\Omega^2}{\bar{\mu}^2r^2}+\frac{\Omega^4}{\bar{\mu}\bar{K}T_0}\right)\psi+(S_\theta+S_T)+(C_\theta+C_T)=0. \tag{5.9}$$

Using the substitutions (4.13) and (4.14), and writing $z=\eta Z$, we obtain

https://doi.org/10.1017/jfm.2011.289 Published online by Cambridge University Press

$$\frac{8\mathscr{A}^8}{\rho_w^2 R^6}\frac{\partial}{\partial\xi}\left(\mathrm{e}^{\xi}\frac{\partial}{\partial\xi}\left(1+\frac{\xi}{\mathscr{A}^2}\right)\frac{\partial}{\partial\xi}\left(\mathrm{e}^{\xi}\frac{\partial\psi}{\partial\xi}\right)\right)+\frac{4\mathscr{A}^4}{\rho_w^2 R^4 Z^2}\frac{\partial}{\partial\xi}\left(\mathrm{e}^{2\xi}\frac{\partial}{\partial\xi}\frac{\partial^2\psi}{\partial\eta^2}\right)$$
$$+\frac{4\mathscr{A}^4}{R^4Z^2}\mathrm{e}^{\xi}\frac{\partial^2}{\partial\xi^2}\left(\mathrm{e}^{\xi}\frac{\partial^2\psi}{\partial\eta^2}\right)+\frac{1}{\rho_w^2Z^4R^2}\frac{\mathrm{e}^{2\xi}}{(1-(\xi/\mathscr{A}^2))}\frac{\partial^4\psi}{\partial\eta^4}$$
$$+\left(\frac{4\Omega^2}{\bar{\mu}^2r^2}+\frac{\Omega^4}{\bar{\mu}\bar{K}T_0}\right)\psi+(S_\theta+S_T)+(C_\theta+C_T)=0. \tag{5.10}$$

The above equation is multiplied by $(\rho_w^2Z^4R^2)$, so that the coefficient of the fourth term, expected to be the largest term in the boundary layer, is 1. The result, expressed in terms of the scaled streamfunction $\psi^*=(\psi/\bar{\mu}Z)$, is

$$\frac{16\mathscr{A}^8Z^4}{R^4}\frac{\partial}{\partial\xi}\left(\mathrm{e}^{\xi}\frac{\partial}{\partial\xi}\left(1-\frac{\xi}{\mathscr{A}^2}\right)\frac{\partial}{\partial\xi}\left(\mathrm{e}^{\xi}\frac{\partial\psi^*}{\partial\xi}\right)\right)+\frac{4\mathscr{A}^4Z^2}{R^2}\frac{\partial}{\partial\xi}\left(\mathrm{e}^{2\xi}\frac{\partial}{\partial\xi}\frac{\partial^2\psi^*}{\partial\eta^2}\right)$$
$$+\frac{4\mathscr{A}^4Z^2}{R^2}\mathrm{e}^{\xi}\frac{\partial^2}{\partial\xi^2}\left(\mathrm{e}^{\xi}\frac{\partial^2\psi^*}{\partial\eta^2}\right)+\frac{\mathrm{e}^{2\xi}}{(1-(\xi/\mathscr{A}^2))}\frac{\partial^4\psi^*}{\partial\eta^4}$$
$$+\left(\frac{4Re^2Z^4}{R^4(1-\xi/\mathscr{A}^2)}+\frac{2Re^2\mathscr{A}^2Pr(1-\gamma^{-1})Z^4}{R^4}\right)\psi^*$$
$$+(S_\theta^*+S_T^*)+(C_\theta^*+C_T^*)=0, \tag{5.11}$$

where

$$S_\theta^*=\frac{8\mathscr{A}^4Re^2Z^4}{R^4}\int_{\eta_0}^{\eta}\mathrm{d}\eta\left(\frac{\partial^2}{\partial\xi^2}((1-\xi/\mathscr{A}^2)^{1/2}\tilde{v}_\theta^*)\right), \tag{5.12}$$

$$C_\theta^*=-\frac{2Re^2Z^2}{R^2}\frac{1}{(1-\xi/\mathscr{A}^2)^{1/2}}\left.\frac{\partial\tilde{v}_\theta^*}{\partial\eta}\right|_{\eta=\eta_0}, \tag{5.13}$$

$$S_T^*=-\frac{4\mathscr{A}^4Re^2Z^4}{R^4}\frac{\partial}{\partial\xi}\left((1-\xi/\mathscr{A}^2)\frac{\partial}{\partial\xi}\left(\int_{\eta_0}^{\eta}\mathrm{d}\eta\tilde{T}^*\right)\right), \tag{5.14}$$

$$C_T^*=\frac{Re^2Z^2}{R^2}\left.\frac{\partial\tilde{T}^*}{\partial\eta}\right|_{\eta=\eta_0}, \tag{5.15}$$

where $\tilde{v}_\theta^*=(\tilde{v}_\theta/\Omega R)$ and $\tilde{T}^*=\tilde{T}/T_0$.

In the generalized Carrier–Maslen approximation for the axial boundary layer, the scaled η coordinate is defined by

$$\eta^*=Re^{1/2}(Z/R)\eta. \tag{5.16}$$

Equation (5.11) is divided throughout by (Re^2Z^4/R^4), to obtain

$$\frac{16\mathscr{A}^8}{Re^2}\frac{\partial}{\partial\xi}\left(\mathrm{e}^{\xi}\frac{\partial}{\partial\xi}\left(1-\frac{\xi}{\mathscr{A}^2}\right)\frac{\partial}{\partial\xi}\left(\mathrm{e}^{\xi}\frac{\partial\psi^*}{\partial\xi}\right)\right)+\frac{4\mathscr{A}^4}{Re^2}\frac{R^2}{Z^2}\frac{\partial}{\partial\xi}\left(\mathrm{e}^{2\xi}\frac{\partial}{\partial\xi}\frac{\partial^2\psi^*}{\partial\eta^{*2}}\right)$$
$$+\frac{4\mathscr{A}^4}{Re^2}\frac{R^2}{Z^2}\mathrm{e}^{\xi}\frac{\partial^2}{\partial\xi^2}\left(\mathrm{e}^{\xi}\frac{\partial^2\psi^*}{\partial\eta^{*2}}\right)+\frac{\mathrm{e}^{2\xi}}{(1-(\xi/\mathscr{A}^2))}\frac{\partial^4\psi^*}{\partial\eta^{*4}}$$
$$+\left(\frac{4}{(1-\xi/\mathscr{A}^2)}+2\mathscr{A}^2Pr(1-\gamma^{-1})\right)\psi^*$$
$$+\frac{R^4}{Z^4Re^2}(S_\theta^*+S_T^*+C_\theta^*+C_T^*)=0. \tag{5.17}$$

https://doi.org/10.1017/jfm.2011.289 Published online by Cambridge University Press

In the generalized Carrier–Maslen equation, the above equation is approximated as

$$\frac{\mathrm{e}^{2\xi}}{(1-(\xi/\mathscr{A}^2))}\frac{\partial^4\psi^*}{\partial\eta^{*4}}+\left(\frac{4}{(1-\xi/\mathscr{A}^2)}+2\mathscr{A}^2Pr(1-\gamma^{-1})\right)\psi^*=0. \tag{5.18}$$

This approximation is valid under the following conditions. The first, second and third terms on the left of (5.17) can be neglected for $(\mathscr{A}^2/Re)\ll 1$. It is easily verified that the terms proportional to S^*_θ and S^*_T in (5.17) scale as $(\mathscr{A}^4R/Re^{1/2}Z)$, while those proportional to C^*_θ and C^*_T scale as $(Re^{1/2}R/Z)$. These can be neglected only in the limit of high aspect ratio and high Reynolds number. Therefore, the generalized Carrier–Maslen equation is valid only when the flow is restricted to a thin boundary layer of thickness $Re^{-1/2}Z$ at the end caps, and the boundary layer thickness $Re^{-1/2}Z$ is much smaller than the cylinder radius R.

The solution for the homogeneous form of the generalized Carrier–Maslen equation is easily obtained in terms of the variable $\eta^\dagger$:

$$\eta^\dagger=\eta^*\{(\mathrm{e}^{(-2\xi)}(4+2\mathscr{A}^2Pr(1-\gamma^{-1})(1-\xi/\mathscr{A}^2)))\}^{1/4}. \tag{5.19}$$

The general solution for the scaled streamfunction in terms of this scaled coordinate is

$$\psi^*=C_1\mathrm{e}^{((1+\mathrm{i})\eta^\dagger/\sqrt{2})}+C_2\mathrm{e}^{(-(1+\mathrm{i})\eta^\dagger/\sqrt{2})}+C_3\mathrm{e}^{((1-\mathrm{i})\eta^\dagger/\sqrt{2})}+C_4\mathrm{e}^{(-(1-\mathrm{i})\eta^\dagger/\sqrt{2})}. \tag{5.20}$$

Since the velocities decay to zero as $z\to\infty$, we can assume without loss of generality that $\psi^*(r,z\to\infty)=0$. Consequently, the constants C_1 and C_3 in (5.20) are both zero.

The velocity components can be expressed in terms of the streamfunction as

$$\begin{aligned}\tilde{v}_r&=-\frac{1}{\rho r}\frac{\partial\psi}{\partial z}\\&=\frac{\bar{\mu}Z}{\bar{\rho}r}\frac{Re^{1/2}}{R}\frac{\partial\psi^*}{\partial\eta^\dagger}\frac{\partial\eta^\dagger}{\partial\eta^*}\\&=\frac{\bar{\mu}Z}{\bar{\rho}r}\frac{Re^{1/2}}{R}\{(\mathrm{e}^{(-2\xi)}(4+2\mathscr{A}^2Pr(1-\gamma^{-1})(1-\xi/\mathscr{A}^2)))\}^{1/4}\frac{\partial\psi^*}{\partial\eta^\dagger}\end{aligned} \tag{5.21}$$

and

$$\begin{aligned}\tilde{v}_z&=\frac{1}{\bar{\rho}r}\frac{\partial\psi}{\partial r}\\&=-\frac{2\mathscr{A}^2\bar{\mu}Z}{\bar{\rho}R^2}\frac{\partial\psi^*}{\partial\xi}\\&=-\frac{2\mathscr{A}^2\bar{\mu}Z}{\bar{\rho}R^2}\frac{\partial\psi^*}{\partial\eta^\dagger}\frac{\partial\eta^\dagger}{\partial\xi}.\end{aligned} \tag{5.22}$$

Equations (5.21) and (5.22) show that both the normal and tangential velocities are proportional to $(\partial\psi^*/\partial\eta^\dagger)$. Therefore, a zero normal velocity (no penetration) condition also implies that the tangential velocity is zero within the context of the generalized Carrier–Maslen approximation; it is necessary to include higher-order corrections to specify the tangential and normal velocities independently. However, this does not turn out to be a restriction in the present case, because the molecular simulations in § 2 show that the tangential velocity at the end caps is numerically small, and the zero normal velocity approximation is a good one for the radial flow at the end caps. The zero normal velocity condition serves to fix one of the constants in

https://doi.org/10.1017/jfm.2011.289 Published online by Cambridge University Press

the solution (5.20). The final constant is fixed from the flux condition,

$$\psi(r, z=\infty) - \psi(r, z=0) = \int_0^\infty r\,\mathrm{d}z\bar{\rho}v_r = \frac{F}{2\pi}, \tag{5.23}$$

where F is the total mass flow rate. This can be expressed in terms of the dimensionless variables as

$$\psi^*(r, z=0) = -\frac{F}{2\pi\bar{\mu}Z}. \tag{5.24}$$

Here, we have assumed that $\psi^*(r, z\to\infty) = 0$ without loss of generality. With this, the final solution for the streamfunction in terms of the flow rate is

$$\psi^* = \frac{F}{2\pi\bar{\mu}Z}\left(\frac{1+\mathrm{i}}{2}\mathrm{e}^{(-(1+\mathrm{i})\eta^\dagger/\sqrt{2})} + \frac{1-\mathrm{i}}{2}\mathrm{e}^{(-(1-\mathrm{i})\eta^\dagger/\sqrt{2})}\right). \tag{5.25}$$

6. DSMC simulation

The direct simulation Monte Carlo method (DSMC) is a numerical method for modelling rarefied gas flows. Here, the Boltzmann equation for the probability distribution function for gas molecules is solved using a probabilistic (Monte Carlo) simulation technique. The Boltzmann equation is more fundamental than the Navier–Stokes equations, since it describes the evolution of the velocity distribution function of the gas molecules. The Navier–Stokes equations are obtained by taking the first, second and third moments of the Boltzmann equation with respect to the molecular velocities. While taking moments, the assumption of 'local equilibrium' (velocity distribution function close to the Maxwell–Boltzmann distribution) is made, thereby restricting the Navier–Stokes equations to near-equilibrium flows. Since there is no assumption of local equilibrium in the Boltzmann equation, it is valid even for far-from-equilibrium flows, provided the molecular chaos approximation is satisfied.

The DSMC method uses 'simulated molecules', which represent a large number of real gas molecules. A basic assumption is that the inter-molecular collisions and molecular motion between collisions can be decoupled over time scales comparable to the time between collisions. The translation of molecules between collisions is deterministically modelled, while the inter-molecular collisions and molecular surfaces are incorporated using probabilistic models. The most common model is the hard-sphere model, but other models such as the variable hard-sphere and variable soft-sphere models are also used in order to accurately reproduce the density and temperature dependence of the viscosity. The hydrodynamic fields (density, velocity, temperature) are obtained by averaging over the molecular distribution functions in the DSMC simulations.

At the boundaries, it is necessary to prescribe interaction laws between the molecules and the solid surfaces. Accurate specification of the interaction laws requires a detailed knowledge of the molecule–surface interaction. However, there are standard interaction laws based on the surface velocity and temperature which are sufficient for predicting the hydrodynamic fields accurately. The most commonly used is the 'diffuse reflection' condition, where a molecule incident on the surface is reflected with a Gaussian velocity distribution with the same mean velocity and temperature as that of the surface. Another commonly used condition is the specular

https://doi.org/10.1017/jfm.2011.289 Published online by Cambridge University Press

reflection condition, that the velocity normal to the surface is reversed while that tangential to the surface is unchanged. It is important to note that these boundary conditions are different from the no-slip conditions in the continuum models. In high-Knudsen-number flows, the diffuse and specular reflection conditions do predict a slip velocity at the surface. From the kinetic theory of dilute gases (Chapman & Cowling 1970), the viscosity of a hard-sphere gas in the dilute limit is given by

$$\mu = \frac{5\sqrt{mk_BT}}{16\sqrt{\pi}d^2}, \tag{6.1}$$

where k_B is the Boltzmann constant, while the speed of sound c_s is given by the relation

$$mnc_s^2 = \gamma p = \gamma n k_B T, \tag{6.2}$$

where m is the molecular mass, n is the number density, and p is the pressure. From this the stratification parameter $\mathscr{A}$, Reynolds number Re, cylinder radius R, molecular diameter (d) and volume fraction of the molecules ϕ are related by the following equation:

$$Re = \frac{96}{5} \times \frac{\sqrt{2}}{\sqrt{\pi}} \mathscr{A} \phi \frac{R}{d}, \tag{6.3}$$

where the volume fraction of the molecules is given by

$$\phi = \frac{\pi}{6} d^3 n, \tag{6.4}$$

where n is the number density of the molecules. The important point to note, from (6.3), is that the Reynolds number is proportional to the stratification parameter times $\phi(R/d)$, where R is the macroscopic scale. Therefore, if we are keeping the volume fraction (density) a constant, increasing (decreasing) the Reynolds number at constant stratification parameter corresponds to increasing (decreasing) the system size R in relation to the molecular diameter.

The details of the DSMC simulation procedure are discussed in Bird (1994), and so we do not repeat the discussion here, but restrict attention to the parameters in the simulations. The number of intervals along the radial direction is 400 with clustering towards the rotating sidewall, while there are 1600, 3200 and 6400 intervals along the axial direction with clustering towards the top and bottom end caps for aspect ratio $Z/D = 2$, 4, and 8 respectively. For the validation of our results with those of Wood & Morton (1980) in the next section, we use the aspect ratio 18.33 that was used in Wood & Morton (1980). For this case alone, the simulation contains 400 intervals in the radial direction and 7200 intervals in the axial direction. The cell width is no greater than one-third of the local mean free path. The number of subcells per cell is taken as 4 for both radial and axial directions. The number of simulated particles per cell is taken as 100. In our simulations, the number of real molecules per simulated particles varied between 10^{16} and 10^{18}.

7. Secondary flow due to wall forcing

The direct simulation Monte Carlo method (DSMC) is used here to simulate the gas flow in the two-dimensional axisymmetric r–z plane. The flow geometry and coordinate system are shown in figure 2(a), and the characteristic streamline plot in figure 2(b). In the case of wall thermal drive, a linear temperature profile is applied

https://doi.org/10.1017/jfm.2011.289 Published online by Cambridge University Press

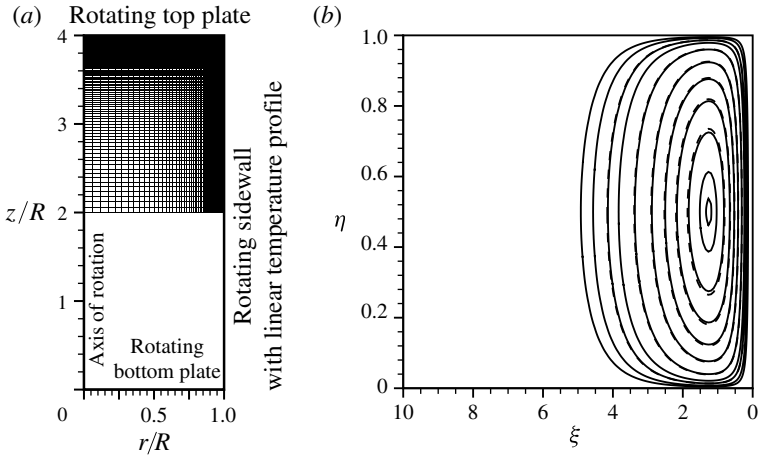


FIGURE 2. Computational domain and coordinate system (with cell arrangement in the flow domain for aspect ratio $Z/D = 2$) (*a*), and characteristic streamline plot for $\mathscr{A} = 3.535$, $Re = 10^4$, $F_T = 0.2$, aspect ratio $Z/D = 4$ (*b*), for the secondary flow with a linear wall temperature profile. The lines show the analytical solution for the generalized Onsager model (−−), and the results of DSMC simulation (—). Here $F_T = (Z/T_0)(\partial T/\mathrm{d}z)$.

along the rotating sidewall. This results in an upward secondary flow along the wall. When the gas reaches the end cap, there is an inward flow along the top end cap, and a simultaneous downward flow in the core of the cylinder. The circulation is completed by an outward flow along the bottom end cap. Simulations were carried out for stratification parameters in the range 0.707–3.535, and Reynolds numbers in the range 10^2–10^6. Three different aspect ratios, $Z/D = 2$, 4 and 8, are considered in the analysis (where Z is the height and D is the diameter of the cylinder). Only the comparisons for $Z/D = 2$ are shown here. This because the high-aspect-ratio limit $Z/D \gg 1$ is made in the analysis, and the smallest aspect ratio provides the most stringent test. For comparison, the scaled wall temperature gradient is defined by

$$F_T = (Z/T_0)(\partial T/\mathrm{d}z), \tag{7.1}$$

where T_0 is the average temperature. The value of F_T provides the magnitude of the perturbation to the base flow due to the wall temperature gradient. Two values of F_T, 0.1 and 0.2 are used in the present analysis.

First, we validate the DSMC simulation results with the earlier results of Wood & Morton (1980) for linear wall thermal drive. The cylinder parameters from the configuration of Wood & Morton (1980) are used for validation: length $L = 3.353$ m, diameter $D = 0.1829$ m, wall pressure $p_w = 13.3$ kPa, peripheral speed $\Omega R = 700$ m s^{-1}, stratification parameter $\mathscr{A} = 5.880$ (assuming speed of sound $c_s = 86.91$ m s^{-1} at 300 K), Reynolds number $Re = 2.4674 \times 10^6$ and average temperature $T_0 = 300$ K. Here, we have chosen the highest peripheral speed of 700 m s^{-1}, to compare the DSMC results with the Onsager and generalized Onsager equations, because the Onsager model becomes more accurate as the peripheral speed increases, or the Reynolds number increases. There is a temperature difference of 1 K between the two ends of the cylinder, and the hotter end is at $\eta = 0$ in our configuration. The temperature profile is assumed to be linear along the rotating sidewall, with the temperature constant on the end caps.

https://doi.org/10.1017/jfm.2011.289 Published online by Cambridge University Press

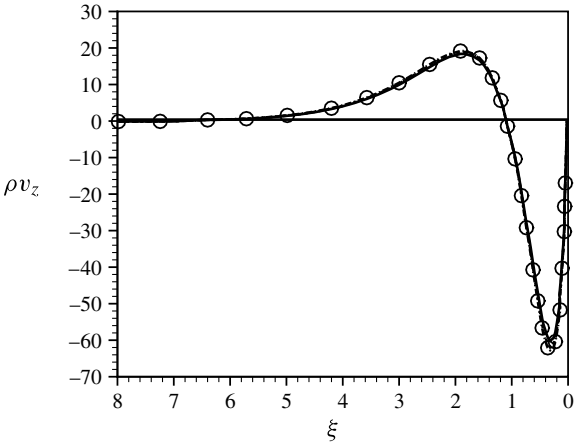


FIGURE 3. Axial mass flux (g m^{-2} s^{-1}) as a function of $\xi = \mathscr{A}^2(1 - (r/R)^2)$ at the axial location $\eta = z/Z = 0.5$ for a linear wall temperature gradient. The cylinder peripheral speed is 700 m s^{-1}, the average temperature is 300 K, and the difference in temperature from end to end is 1 K. The lines show the results of Wood & Morton (1980) (—), the Onsager model with no slip (− −), the generalized Onsager model with no slip (· − ·), while the symbol (○) shows the DSMC results.

The gas used in the simulations of Wood & Morton (1980) was Uranium hexafluoride (UF_6) gas. For this gas, the molecular mass $58.442\,636 \times 10^{-26}$ kg molecule^{-1}, molecular diameter $= 5.5 \times 10^{-10}$ m, viscosity index 0.933, and ratio of specific heats 1.066 are obtained from Villani (1979). It is assumed that the gas molecules undergo diffuse reflection from all the solid surfaces with the thermal accommodation coefficient equal to 1. The time step in the simulation is chosen to be small compared to the time between collisions. The mean collision time is calculated to be $t = (\lambda/c_{av})$, where λ is the mean free path and c_{av} is the average molecular velocity. The minimum value of the mean free path at the rotating sidewall, calculated from the gas density at the wall, is $\lambda = 2.316\,742 \times 10^{-7}$ m. The average molecular velocity is calculated as $\sqrt{k_B T/m} = 84.177\,17$ m s^{-1}. This gives the mean collision time $t = 2.752\,221 \times 10^{-9}$ s. The time step used in the simulations is 5.0×10^{-10} s, which is less than the mean collision time.

A comparison of axial mass flux, expressed in g m^{-2} s^{-1}, as a function of ξ at the axial location $\eta = 0.5$, for peripheral speed 700 m s^{-1} with the earlier result of Wood & Morton (1980), is shown in figure 3. This shows that the present DSMC simulations are in agreement with the analytical solutions for the high-stratification-parameter and high-Reynolds-number limit.

In order to check the convergence of the simulations, we have varied both the time step and the number of simulated molecules per cell, keeping the number of real molecules a constant. In all cases, the time step is decreased by a factor of 5 and the number of simulated molecules increased by a factor of 2 for the parameters where the amplitude of the secondary flow is the largest, and verify that there is less than 1 % change in the resulting secondary flow profiles. The comparisons for a linear wall temperature profile with $Z/D = 2$, $Re = 10^2$, $\mathscr{A} = 1.414$ and $F_T = 0.2$ is shown in figure 4. Different time steps (5×10^{-10}, 1×10^{-9}, 1.5×10^{-9} s) and different numbers of simulated molecules per cell (100, 80, 60) are used to test the convergence. It is found that for the parameters corresponding to the largest secondary flow amplitude,

https://doi.org/10.1017/jfm.2011.289 Published online by Cambridge University Press

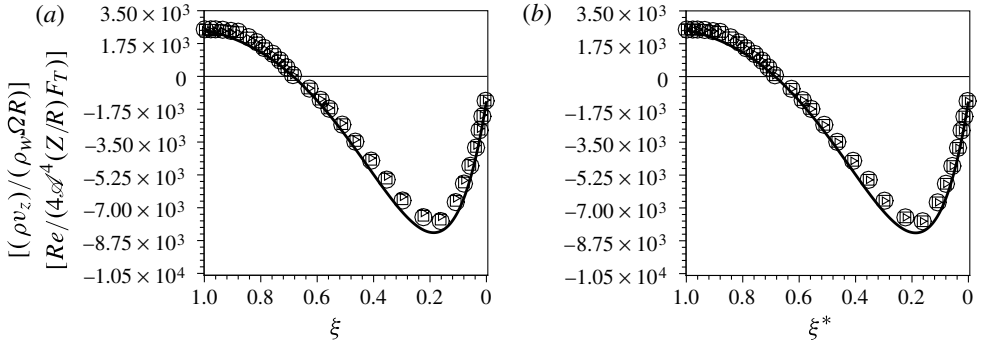


FIGURE 4. Axial mass flux, scaled by $(\rho_w \Omega R)$, $(4\mathscr{A}^4(Z/R)F_T/Re)$, as a function of ξ^* at $\eta = 0.5$, aspect ratio $Z/D = 2$, for $\mathscr{A} = 1.414$, $Re = 10^2$, $F_T = 0.2$. (*a*) Different time steps t in seconds. The symbols show the DSMC results for $t = 5 \times 10^{-10}$ (○), $t = 1 \times 10^{-9}$ (□), $t = 1.5 \times 10^{-9}$ (△). (*b*) Different numbers of simulated molecules per cell n_s. The symbols show the DSMC results for $n_s = 100$ (○), $n_s = 80$ (□), $n_s = 60$ (△). The line shows the generalized Onsager model with slip (—).

the results are insensitive to the time step and the number of molecules per cell. This clearly shows the convergence of the simulation results. Similar results are obtained for mass and momentum sources within the flow, but we do not provide the details here.

7.1. *Linear wall temperature gradient*

The analytical solutions, obtained by solving the Onsager and generalized Onsager equations for linear wall thermal drive, are compared with two-dimensional axisymmetric DSMC simulations. In the simulations, the temperature difference applied along the rotating sidewall is independent of the aspect ratio, so that the temperature gradient is inversely proportional to the aspect ratio. Therefore, the system with the smallest aspect ratio has the highest temperature gradient. Although the imposed temperature along the wall varies linearly with height, our results showed that the gas temperature at the wall is different, by a maximum of ∼15–20 %, from the wall temperature. It should be noted that the temperature of the gas is not fixed at the wall in the simulations; rather, the gas temperature is set by the diffuse reflection condition, with the reflected molecules having the same temperature as the wall. Consequently, the average temperature of the gas molecules after collision is equal to the wall temperature, but the average temperature of molecules before collision is not. This results in a significant 'temperature slip' at the wall, as shown in figure 5(*a*,*b*). Since the solutions in (4.45) and (4.50) were obtained for a linear variation in the temperature gradient with height, we use the linear approximation for the temperature gradient, shown in figure 5(*a*,*b*) for our comparison. The temperature slip has very little variation with Reynolds number, though it does increase with stratification parameter.

In the simulations, it was verified that the temperature slip is a non-continuum effect consistent with the temperature variation in the radial direction, as follows. The average temperature of a molecule reflected from the wall is equal to the wall temperature, T_w. The average temperature of a molecule hitting the wall depends on the temperature at the radial position where the molecule had its most recent collision. In order to calculate this, we determine the probability distribution $P_o(r)$, which is

https://doi.org/10.1017/jfm.2011.289 Published online by Cambridge University Press

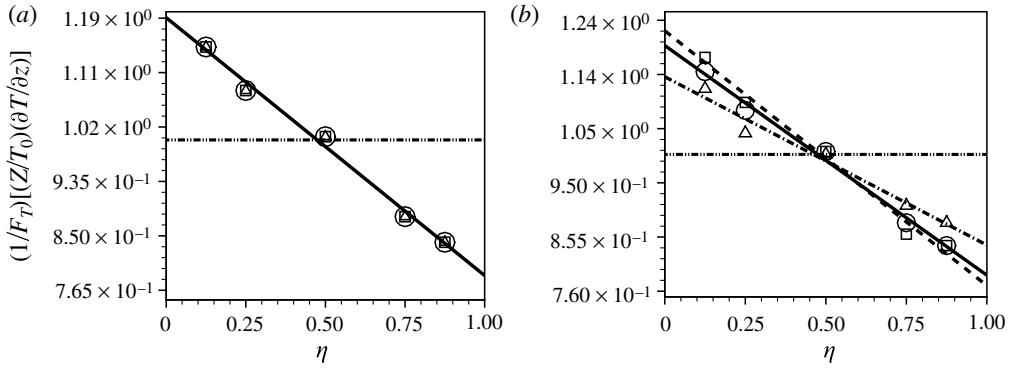


FIGURE 5. Variation of scaled temperature gradient of the gas at the wall with axial coordinate $\eta = z/Z$, scaled temperature gradient $F_T = 0.2$, and for different Reynolds numbers and stratification parameters. The lines show the applied wall temperature gradient ($\cdot\cdot-\cdot\cdot$), the linear temperature gradient used in the generalized Onsager model for $\mathscr{A} = 0.707$ ($\cdot - \cdot$), $\mathscr{A} = 2.121$ (—) and $\mathscr{A} = 3.535$ (−−). (*a*) Variation with Reynolds number at $\mathscr{A} = 2.121$, $Re = 10^2$ (○), $Re = 10^4$ (□), and $Re = 10^6$ (△). (*b*) Variation with stratification parameter at $Re = 10^6$, $\mathscr{A} = 3.535$ (□), $\mathscr{A} = 2.121$ (○), $\mathscr{A} = 0.707$ (△).

defined such that $P_o(r)\,\mathrm{d}r$ is the probability that the molecule hitting the wall had its most recent collision in the interval $\mathrm{d}r$ about the location r. The probability $P_o(r)$ is normalized so that $\int_0^R \mathrm{d}r\, P_o(r) = 1$. The average temperature of the molecules incident on the wall is then

$$T_i = \int_0^R \mathrm{d}r\, P_o(r) T(r). \tag{7.2}$$

For consistency, it is necessary that the gas temperature at the wall, T_{gw}, is the average temperature of the molecules incident and reflected, that is,

$$T_{gw} = (T_i + T_w)/2, \tag{7.3}$$

where T_w is the wall temperature. In the numerical simulations, we have independently verified that T_{gw} calculated from (7.2) and (7.3) is equal to that actually measured in the simulations at the wall. An example of this is shown in figures 6 and 7, where we have plotted both $P(\xi^*)$ and $T(\xi^*)$ as a function of ξ^*, where $\xi^* = \xi/\mathscr{A}^2$.

We also find that there is a substantial velocity slip at the wall. To a good approximation, the slip velocity is proportional to the Reynolds number, and it decreases as the stratification parameter is increased, and is proportional to the scaled temperature gradient F_T (equation (7.1)). This is shown in figure 8(*a*), where the axial velocity at the rotating sidewall, non-dimensionalized by $R\Omega$ and scaled by F_T, is plotted as a function of stratification parameter at the axial location $\eta = 0.5$. It is also observed from figure 8(*a*) that the scaled slip velocity, divided by $R\Omega F_T$, shows remarkably little dependence on the Reynolds number. In the case of inflow/outflow of gas along the axis, the dimensionless scaled feed rate is defined by

$$F^* = F/(H\Omega), \tag{7.4}$$

where F is the feed rate, H is the total gas holdup and Ω is the angular velocity. The scaled feed rate is a measure of the perturbation to the base flow due to external feed. In figure 8(*b*), the axial velocity at the rotating sidewall, non-dimensionalized

https://doi.org/10.1017/jfm.2011.289 Published online by Cambridge University Press

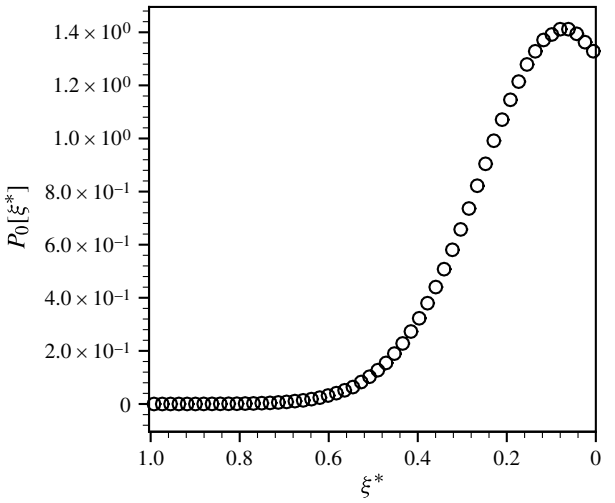


FIGURE 6. The probability distribution $P_o(\xi)$ as a function of ξ^* at $\eta = 0.25$ for $\mathscr{A} = 2.121$, $Re = 10^6$, aspect ratio $Z/D = 2$ and scaled wall temperature gradient $F_T = 0.1$.

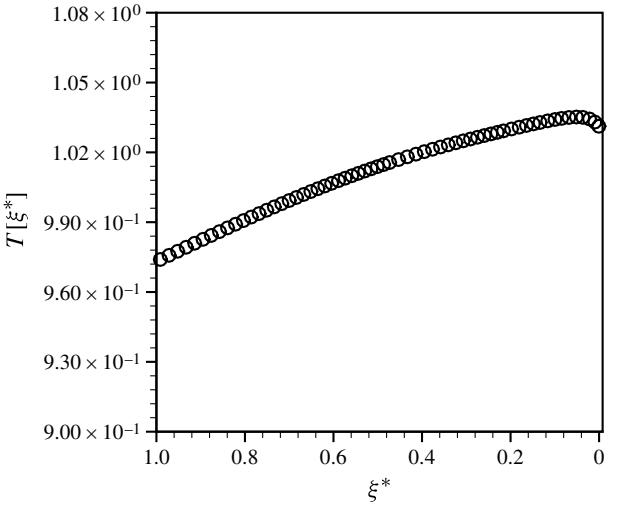


FIGURE 7. Temperature distribution as a function of ξ^* at $\eta = 0.25$ for $\mathscr{A} = 2.121$, $Re = 10^6$, aspect ratio $Z/D = 2$, and scaled wall temperature gradient $F_T = 0.1$.

by $R\Omega$ and scaled by F^*, is plotted as a function of stratification parameter at the axial location $\eta = 0.675$ for inflow/outflow of gas along the axis.

The axial mass flux, non-dimensionalized by $\rho_w \Omega R$, is plotted at $\eta = 0.5$, as a function of ξ^* for different stratification parameters $\mathscr{A} = 3.535$, 2.121, 1.414 and 0.707, for two different values $F_T = 0.1$ and 0.2, and for Reynolds numbers 10^2 and 10^4 in figure 9. It is convenient to multiply the flux by the factor $(4\mathscr{A}^4(Z/R)F_T/Re)$, so that the analytical result is independent of Reynolds number, scaled temperature gradient F_T and aspect ratio, and they depend only on the stratification parameter. It should be noted the large numerical value is due to the scaling used for the flux; if the

https://doi.org/10.1017/jfm.2011.289 Published online by Cambridge University Press

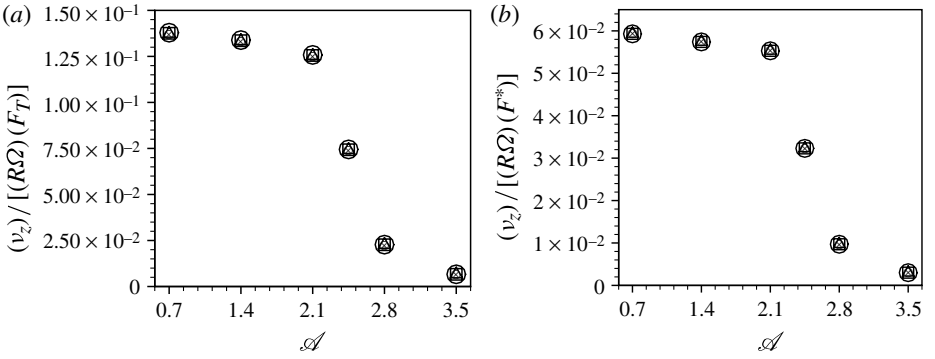


FIGURE 8. Axial slip velocity at the curved surface, scaled by $R\Omega F_T$ and $R\Omega F^*$, respectively, for wall thermal forcing at $\eta = 0.5$ (a) and mass inflow/outflow along the axis at $\eta = 0.675$ (b) as a function of $\mathscr{A}$, aspect ratio $Z/D = 2$. The symbols show the DSMC results for $Re = 10^4$, $F_T/F^* = 0.1$ ($\otimes$), $Re = 10^4$, $F_T/F^* = 0.2$ ($\triangle$), $Re = 10^2$, $F_T/F^* = 0.1$ ($\square$), $Re = 10^2$, $F_T/F^* = 0.2$ ($\circ$). Here $F_T = (Z/T_0)(\partial T/\mathrm{d}z)$, and $F^* = F/(H\Omega)$.

flux is expressed in unscaled form, the maximum value of (flux/$\rho_w \Omega R$) is 0.211 0028 (for $\mathscr{A} = 0.707$).

There is quantitative agreement (with a difference of less than 5 %) between the predictions of the analytical model (generalized Onsager model with slip) and the DSMC simulations even when the secondary flow is as large as the $F_T = 0.2$, the stratification parameter is 0.707, the Reynolds number is 100 and the cylinder length is twice the diameter, provided the velocity and temperature slip are incorporated in the analytical model. The agreement is not as good if the slip is not incorporated in the generalized Onsager model, while the agreement is poor for the original Onsager model for $\mathscr{A} = 0.707$, 1.414 and 2.121. This shows that the generalized Onsager model captures the secondary flows quantitatively even at stratification parameter as low as 0.707, provided the boundary conditions in the analytical model are accurately specified.

7.2. *Inflow/outflow along the axis*

The flow geometry and coordinate system for inflow/outflow of gas along the axis is shown in figure 10(a) and characteristic streamlines are shown in figure 10(b). The gas is introduced at the axis of the cylinder at $\eta = 0.5$ and $r = 0$. The gas flows radially outward due to the centrifugal acceleration, and then splits at the wall into two streams, one going upward along the upper half and the other going downward along the lower half. At the two end caps, there is a radially inward flow towards the centre, and the gas is taken out at two locations along the axis, one at the ($\eta = (z/Z) = 0.15$) and the other near the top end cap ($\eta = (z/Z) = 0.85$). Here, Z is the total cylinder height and z is the axial distance from the bottom end cap.

Here, we have carried out simulations for $F^* = 0.1$ and 0.2. The actual feed rate F is varied in such a way that the desired scaled feed rate is obtained at different stratification parameters, Reynolds numbers and aspect ratios.

Substantial axial velocity slip at the rotating sidewall is obtained in the simulations in this case as well. The axial velocity at the rotating sidewall, non-dimensionalized by $F^*R\Omega$, is plotted as a function of stratification parameter at the axial location $\eta = 0.675$ as shown in figure 8(b). It is observed that the slip velocity increases as the

https://doi.org/10.1017/jfm.2011.289 Published online by Cambridge University Press

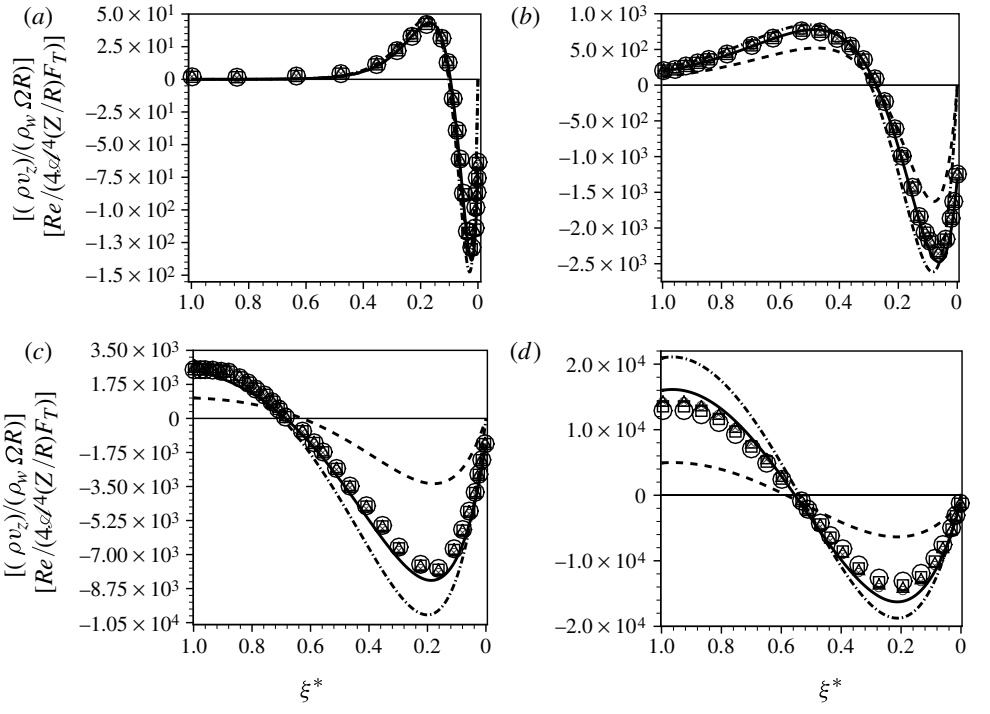


FIGURE 9. Axial mass flux, scaled by $(\rho_w \Omega R)$, $(4\mathscr{A}^4(Z/R)F_T/Re)$, as a function of ξ^* at $\eta = 0.5$, aspect ratio $Z/D = 2$, for $\mathscr{A} = 3.535$ (a), $\mathscr{A} = 2.121$ (b), $\mathscr{A} = 1.414$ (c) and $\mathscr{A} = 0.707$ (d). The symbols show the DSMC results for $Re = 10^4$, $F_T = 0.1$ (⊗); $Re = 10^4$, $F_T = 0.2$ (△); $Re = 10^2$, $F_T = 0.1$ (□); $Re = 10^2$, $F_T = 0.2$ (○). The lines are the generalized Onsager model with slip (—), the generalized Onsager model with no slip $(\cdot - \cdot)$, and the Onsager model with no slip $(--)$.

Reynolds number and F^* are increased, and slip velocity decreases as the stratification parameter is increased.

The analytical solutions are compared with the results of DSMC simulations in figure 11. The trends are consistent with those for the wall thermal drive. When the slip velocity and temperature are correctly incorporated in the analytical solution, the results are in quantitative agreement with simulations even when the stratification parameter is as low as 0.707 and the Reynolds number is as low as 100. The generalized Onsager model without wall slip is clearly not in quantitative agreement, even though the trends are broadly consistent. The original Onsager model shows poor agreement, even when the stratification parameter is 2.121, even though the agreement is good at a stratification parameter of 3.535. This clearly indicates that even though the original Onsager model is valid at high stratification parameters, it cannot be extended to moderate stratification parameters. This disadvantage is removed in the generalized Onsager model, where quantitative agreement is obtained even when the stratification parameter is 0.707.

7.3. *Radial flow at end caps*

The analytical solutions obtained by solving the Carrier–Maslen and generalized Carrier–Maslen equations are compared with the results of DSMC simulations. As

https://doi.org/10.1017/jfm.2011.289 Published online by Cambridge University Press

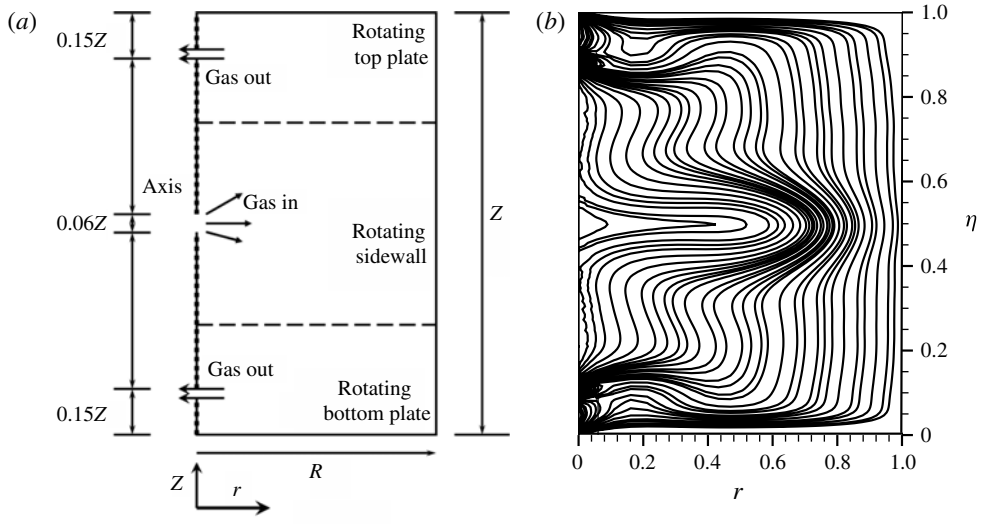


FIGURE 10. Computational domain and coordinate system (*a*) and characteristic streamline plot from DSMC simulation at $\mathscr{A} = 3.535$, $Re = 10^4$, $F^* = 0.2$, aspect ratio $Z/D = 4$ (*b*) for mass inflow/outflow along the axis of the cylinder.

discussed below, it is necessary to specify the total mass flow rate at a fixed radial location in order to obtain the analytical solution. This mass flux is a constant inflow/outflow along the axis, because there is an upward flow along the wall in the upper half, an inward flow along the end caps and removal of gas at the axis of the cylinder. In the case of the linear temperature gradient, there is an upward flow of gas along the wall in the upper half, and simultaneous inward and downward flow along the top end cap. Due to this, the radial mass flow rate varies with position, and the constant mass flux condition cannot be used to obtain the generalized Carrier–Maslen equations. Therefore, we compute the end-cap solutions only for the secondary flow due to a mass source. The wall slip velocity, which was an important factor in our analysis of the axial flow, turns out not to be significant for the end caps. The maximum scaled slip velocity (scaled by $(R\Omega)$) obtained in our simulation is 5.0×10^{-4}.

The boundary conditions in the generalized Carrier–Maslen solution are specified as follows. The structure of the generalized Carrier–Maslen solution is such that the leading-order tangential and normal velocities are proportional to each other. Therefore, the no-penetration (zero normal velocity) condition results in the tangential velocity at the surface also being zero. The solution for the streamfunction is then completely determined from the total radial flow rate at the end caps,

$$\psi^*(r, z = 0) = -\frac{F}{2\pi\bar{\mu}Z}, \tag{7.5}$$

with

$$\psi^*(r, z \to \infty) = 0, \tag{7.6}$$

where ψ^* is the scaled streamfunction $\psi/(\bar{\mu}Z)$, and F is the mass flow rate. With the above two conditions, as well as the zero normal velocity condition, the analytical solution for the radial flow at the end caps is completely specified.

https://doi.org/10.1017/jfm.2011.289 Published online by Cambridge University Press

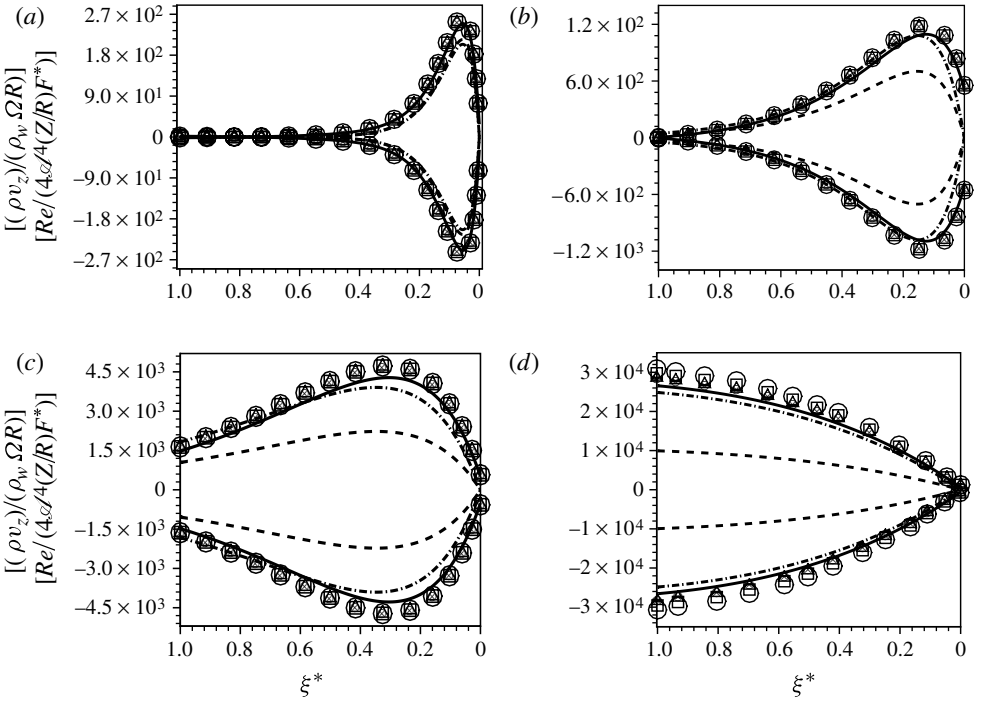


FIGURE 11. Axial mass flux, scaled by $(\rho_w \Omega R)$, $(4\mathscr{A}^4(Z/R)F^*/Re)$, as a function of ξ^* at $\eta = 0.325$ and 0.675 for aspect ratio $Z/D = 2$, and stratification parameter $\mathscr{A} = 3.535$ (a), $\mathscr{A} = 2.121$ (b), $\mathscr{A} = 1.414$ (c) and $\mathscr{A} = 0.707$ (d). The symbols show the DSMC results for $Re = 10^4$, $F^* = 0.1$ ($\otimes$), $Re = 10^4$, $F^* = 0.2$ ($\triangle$), $Re = 10^2$, $F^* = 0.1$ ($\square$), $Re = 10^2$, $F^* = 0.2$ ($\circ$). The lines show the generalized Onsager model with slip (—), the generalized Onsager model with no slip ($\cdot - \cdot$), and the Onsager model with no slip ($--$).

The radial velocity at the end caps, non-dimensionalized by $R\Omega$, is plotted as a function of scaled axial coordinate η^* at $\xi^* = 0.1$, 0.2 and 0.5 in figure 12. The simulation results show that the slip in the tangential velocity at the end caps is numerically small. We find the maximum scaled slip velocity (scaled by $R\Omega$) to be 5.0×10^{-4}. Figure 12 shows that the highly confined boundary layer flow with a small boundary layer thickness close to the cylindrical wall at $\xi^* = 0.1$ expands out due to a flow with lower velocity and higher boundary layer thickness at $\xi^* = 0.5$. Note that for the lowest Reynolds number of 100, the width of the flow in figure 12 extends up to $\eta^* = 5$, or up to 0.5 times the cylinder radius. Even for such a large boundary layer thickness, there is quantitative agreement between the analytical results for the generalized Carrier–Maslen model and the DSMC simulations even for $\mathscr{A} = 0.707$. The original Carrier–Maslen solution does reproduce the trends seen in the simulations, but the agreement is not quantitative.

8. Internal sources

The internal sources of mass, momentum and energy are incorporated in the DSMC simulations as follows. A small circular source domain of radius 10^{-3} times the cylinder radius R is selected for adding/removing mass, momentum and energy. In the case of mass source, a molecule is added at random into the source domain at fixed

https://doi.org/10.1017/jfm.2011.289 Published online by Cambridge University Press

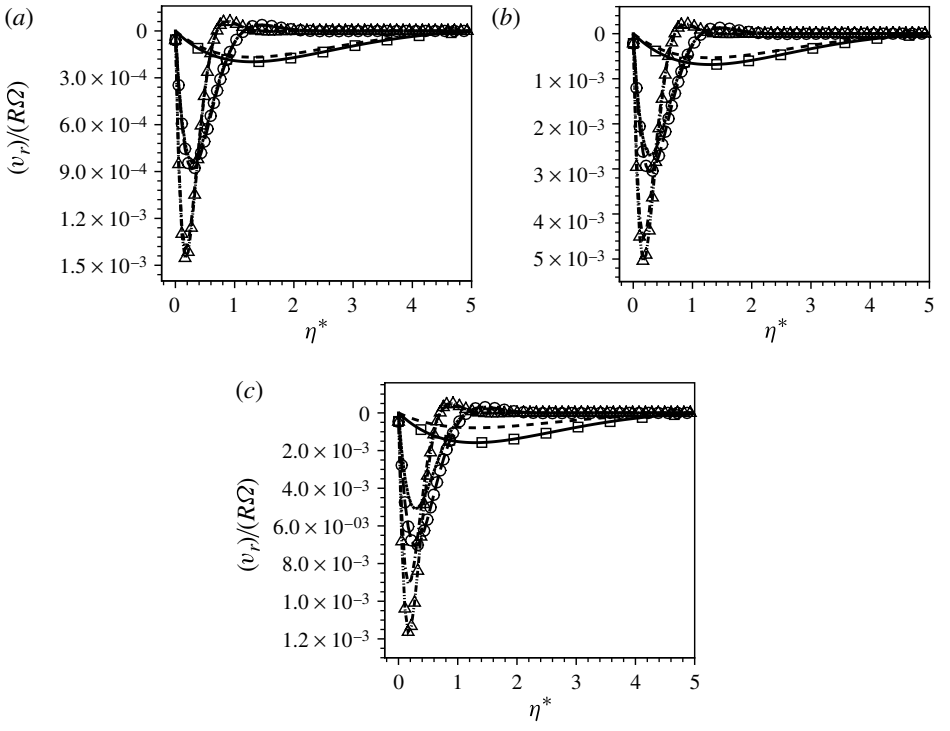


FIGURE 12. Radial velocity, scaled by $R\Omega$, as a function of scaled axial coordinate η^* at $\xi^* = 0.1$ and 0.5, for aspect ratio $Z/D = 2$, for $Re = 100$, $F^* = 0.2$, and $\mathscr{A} = 3.535$ (*a*), $\mathscr{A} = 2.121$ (*b*), and $\mathscr{A} = 0.707$ (*c*). The symbols show the DSMC results for $\xi^* = 0.1$ (△), $\xi^* = 0.2$ (○) and $\xi^* = 0.5$ (□), and the lines are the results at $\xi^* = 0.1$ for the generalized Carrier–Maslen model with no slip ($\cdot\cdot-\cdot\cdot$), the Carrier–Maslen model with no slip ($\cdot-\cdot$); at $\xi^* = 0.2$ for the generalized Carrier–Maslen model with no slip ($--$), the Carrier–Maslen model with no slip ($\cdots$); at $\xi^* = 0.5$ for the generalized Carrier–Maslen model with no slip (—), the Carrier–Maslen model with no slip ($--$).

time intervals determined by the desired rate of mass input. The velocity of the added molecules is chosen from a random Gaussian distribution with the same mean velocity and temperature as that of the gas in the domain. When a molecule is added, the mean velocity and the fluctuating velocity of all other molecules in the domain are scaled by a constant factor so that the total momentum and energy of all the molecules in the source domain remain unchanged due to the addition of a molecule. In the case of a mass sink, molecules are removed at random from the domain at time intervals fixed by the desired rate of mass output. When a molecule is removed, the mean and the fluctuating velocity of all other molecules in the source domain are scaled by a constant factor so that the total momentum and energy in the domain remain unchanged.

Forces (momentum sources) exerted on the gas due to stationary inserts are modelled by imposing impulses (increasing the momentum) of all the molecules in the direction of a force at each collision step. The magnitude of the impulse is determined such that the ratio of the impulse and the time between collisions is equal to the applied force. A localized energy source, which increases or decreases the temperature of the gas, is imposed by scaling the fluctuating velocity of all the molecules in the

https://doi.org/10.1017/jfm.2011.289 Published online by Cambridge University Press

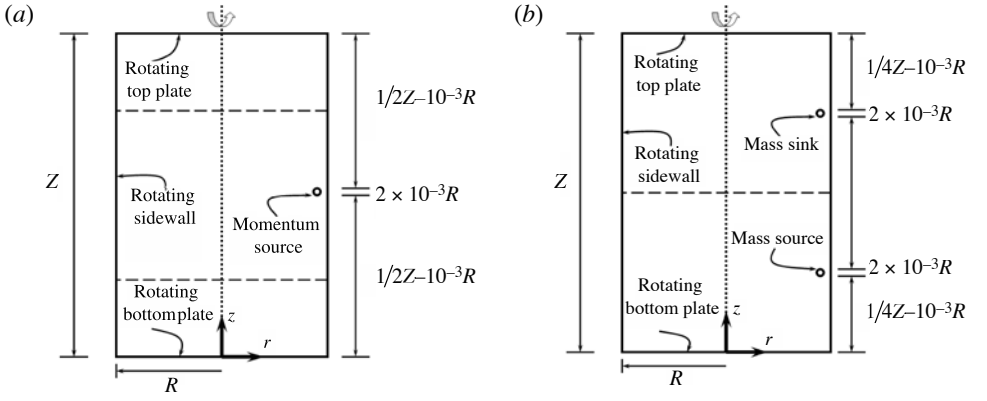


FIGURE 13. Computational domain and coordinate system for (*a*) azimuthal-momentum source at $\eta = 0.5$, and (*b*) mass source at $\eta = 0.25$, and mass sink at $\eta = 0.75$.

source domain. The scaling of the velocity is determined such that the increase in energy divided by the time between collisions is equal to the desired energy input rate.

The relative placement of sources and sinks is identical to that of Wood & Sanders (1983). This enables us to first validate our results with the earlier results based on the Onsager model, and then to extend the study to lower values of Reynolds number, stratification parameter and aspect ratio. There are two different configurations used in Wood & Sanders (1983). The first is a source of angular momentum within the flow at $\eta = 0.5, \xi = 8$, and the second is a mass source at $\eta = 0.25, \xi = 8$ coupled with a mass sink at $\eta = 0.75, \xi = 8$. These are idealized as delta functions in the analytical solution, while in the DSMC simulations, these are formulated as uniform sources over a source domain of radius $10^{-3}R$ centred at the source location, as discussed above. The sources/sinks in Wood & Sanders (1983) were all located outside the radial boundary layer at $\xi = 8$. In our calculation, we place the sources/sinks at two locations, one outside the radial boundary layer at $\xi_s^* = 0.25$, and the second inside the radial boundary layer at $\xi_s^* = 0.01$, where $\xi^* = \xi/\mathscr{A}^2$. The flow geometry and coordinate system are shown in figure 13(*a*) for the momentum source, and in figure 13(*b*) for mass source/sink.

The results of our analytical solution and DSMC simulation are validated against the earlier result of Wood & Sanders (1983) in figure 14(*a*,*b*). This shows that the present simulations are in agreement with the analytical solutions of both the Onsager model and the generalized Onsager model in the high-stratification-parameter and high-Reynolds-number limit.

8.1. *Momentum source*

The influx of momentum/energy near the wall is imposed by increasing the mean/fluctuating velocity of the molecules at the location. When the location is near the wall, the molecules with augmented momentum/energy from the source collide with the wall and locally increase the temperature. This results in a non-zero temperature perturbation at the wall, as shown by the symbols in figure 15(*a*), for $\mathscr{A} = 3.535$ and $Re = 10^2$. Here, the dimensionless temperature slip T_s^* is defined by

$$T_s^* = (T - T_a)/T, \tag{8.1}$$

https://doi.org/10.1017/jfm.2011.289 Published online by Cambridge University Press

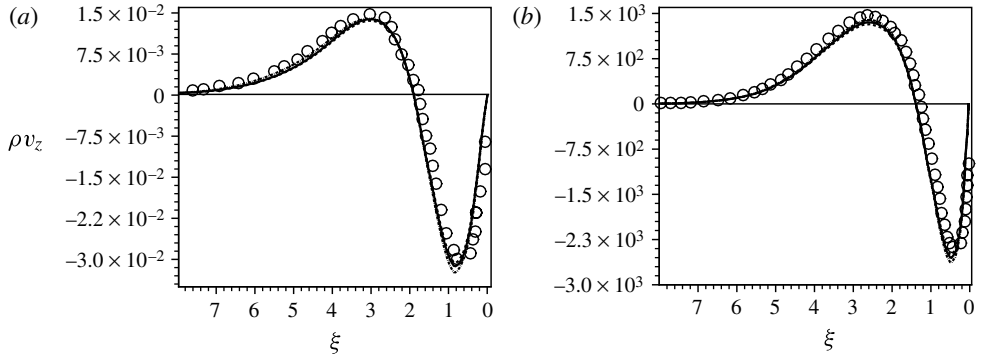


FIGURE 14. Axial mass flux (g m^{-2} s^{-1}) as a function of ξ (*a*) at the axial location $\eta = 0.25$ for the flow induced by azimuthal-momentum source of 1 dyn at $\xi = 8$, $\eta = 0.5$; and (*b*) at the axial location $\eta = 0.5$ for the flow induced by a mass source of 1 gm s^{-1} at $\xi = 8$, $\eta = 0.25$ and a mass sink of 1 gm s^{-1} at $\xi = 8$, $\eta = 0.75$. The lines show the results of Wood & Sanders (1983) (—), the Onsager model with no slip (− −), and the generalized Onsager model with no slip (· − ·), and the (○) symbols show the DSMC results.

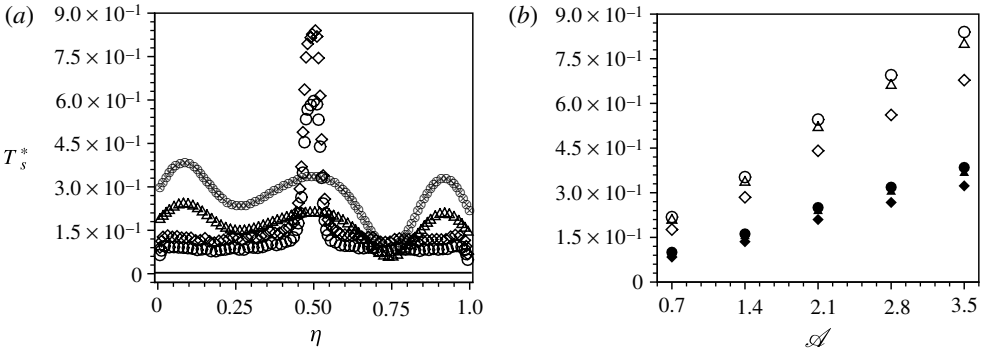


FIGURE 15. Scaled temperature slip T_s^* at the curved wall of the cylinder as a function of η at $Re = 10^2$ (*a*), and the maximum temperature slip as a function of stratification parameter (*b*). In panel (*a*), the symbols show the DSMC results without energy removal for $\mathscr{A} = 3.535$ and source location $\xi_s^* = 0.25$ (○) and $\xi_s^* = 0.01$ (◇) for momentum source, and source location $\xi_s^* = 0.25$ (△) and $\xi_s^* = 0.01$ (⊗) for mass source/sink. The line (—) shows the result with energy removal. In panel (*b*), the maximum temperature slip is shown as a function of stratification parameter, source location $\xi_s^* = 0.01$ for momentum source, and for $Re = 10^6$ (◇), $Re = 10^4$ (△), $Re = 10^2$ (○); and for mass source/sink, $Re = 10^6$ (♦), $Re = 10^4$ (▲), $Re = 10^2$ (●).

where T is the gas temperature at the wall obtained from DSMC simulation, and T_a is the constant gas temperature at the wall assumed in the analytical solution.

The temperature slip violates the homogeneous (zero temperature perturbation) boundary condition used in the analytical solution, as shown in figure 15. At the wall nearest the source, there is an increase of close to 90 % in the temperature at the wall. As we see a little later, this results in a substantial change in the secondary flow. In order to mimic the homogeneous boundary condition for the gas temperature assumed in the analysis, it is necessary to remove energy from the wall. This is done

https://doi.org/10.1017/jfm.2011.289 Published online by Cambridge University Press

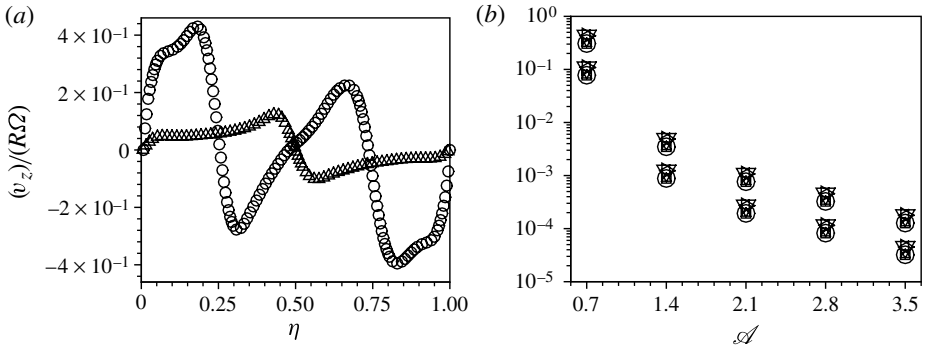


FIGURE 16. Scaled axial slip velocity. In panel (*a*), slip velocity is plotted along the axial coordinate η for momentum source (△) and mass source/sink (○), with source location $\xi_s^* = 0.01$ at $Re = 10^6$ and $\mathscr{A} = 0.707$. In panel (*b*), axial velocity slip at the rotating sidewall, scaled by $R\Omega$, as a function of $\mathscr{A}$, is plotted at $\eta = 0.434\,44$ (maximum slip) for the momentum source shown in figure 13(*a*), and at $\eta = 0.180\,88$ (maximum slip) for the mass source/sink shown in figure 13(*b*). In panel (*b*), the symbols show the DSMC results for $Re = 10^6$, $\xi_s^* = 0.25$ (○), $Re = 10^4$, $\xi_s^* = 0.25$ (□), $Re = 10^2$, $\xi_s^* = 0.25$ (△), $Re = 10^6$, $\xi_s^* = 0.01$ (▽), $Re = 10^4$, $\xi_s^* = 0.01$ (▷), $Re = 10^2$, $\xi_s^* = 0.01$ (◁). The upper symbols for mass source/sink, and lower symbols for momentum source.

by reducing the wall temperature as explained in the simulation section, and the gas temperature at the wall obtained in this manner is shown in figure 15(*a*).

We have also examined, in detail, the velocity slip at the rotating sidewall in the DSMC simulations. The variation of velocity slip for momentum source and mass source/sink inside the radial boundary layer is shown in figure 16 for the momentum source with configuration shown in figure 13(*a*), and for the mass source/sink configuration shown in figure 13(*b*). We find that the slip velocity increases as the Reynolds number is increased and as the stratification parameter is decreased for these cases, and is at a maximum for $Re = 10^6$ and stratification parameter $\mathscr{A} = 0.707$, shown in figure 16(*a*). The maximum slip velocity is close to 0.1 times the mean velocity at $\eta = 0.45$ and 0.55 for the momentum source in figure 16(*a*), and is close to 0.4 times the mean rotational velocity at $\sim\eta = 0.18$ and $\eta = 0.82$ for the mass source and sink. The variation of the maximum slip velocity with Reynolds number and stratification parameter is shown in figure 16(*b*), for two radial locations, $\xi_s^* = 0.01$ inside the boundary layer and $\xi_s^* = 0.25$ outside the boundary layer. As expected, the slip velocity is larger when the source is placed inside the boundary layer. There is very little variation in the slip velocity with Reynolds number, but there is a systematic decrease in the slip velocity as the stratification parameter is increased. In all cases, the largest slip velocity is ∼0.1 times ΩR when the scaled secondary flow rate is 0.2 times that of the primary rotation rate, and it decreases as the stratification parameter is increased.

The analytical solutions are compared with the results of DSMC simulations, where we have taken the precautions discussed above to ensure that homogeneous boundary conditions are satisfied, and incorporating the velocity slip at the wall. The analytical solutions are obtained by considering (*a*) homogeneous boundary condition with internal source, and (*b*) inhomogeneous velocity slip boundary condition with no internal source. The final solution is obtained by superposition of (*a*) and (*b*). Once the homogeneous temperature boundary condition is satisfied at the wall, and

https://doi.org/10.1017/jfm.2011.289 Published online by Cambridge University Press

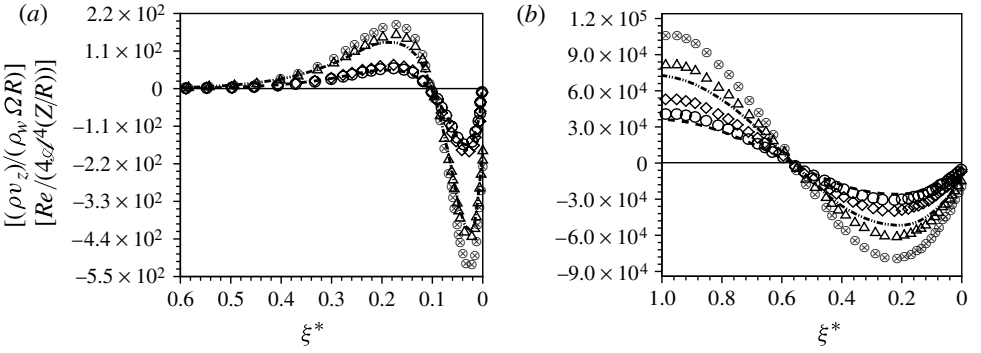


FIGURE 17. Axial mass flux, scaled by $(\rho_w \Omega R)$, $(4\mathscr{A}^4(Z/R)/Re)$, as a function of ξ^* for (a) $\mathscr{A} = 3.535$; (b) $\mathscr{A} = 0.707$ for $Re = 10^2$, aspect ratio $Z/D = 2$, and with source at radial location $\xi_s^* = 0.01$, and source strength $F^* = 0.2$. The symbols show the DSMC results for the axial location $\eta = 0.25$ with energy removal ($\circ$) and without energy removal ($\diamond$), and the axial location $\eta = 0.45$ with energy removal ($\triangle$) and without energy removal ($\otimes$). The solutions of the generalized Onsager model with slip at $\eta = 0.25$ ($--$) and at $\eta = 0.45$ ($\cdots\!-\!\cdots$) are also shown.

the velocity slip is incorporated, it is observed that there is quantitative agreement between the analytical and simulation results as shown in figure 17(*a*,*b*), even at the location $\eta = 0.45$ where the velocity slip is close to maximum. It is observed that near the source $\eta = 0.45$, the magnitude of the slip velocity is high and decreases as we move away from the source $\eta = 0.25$ as shown in figure 17(*a*,*b*). It is also observed that the magnitude of the axial mass flux decays rapidly from the location of the source. Figure 17 also shows that when the homogeneous boundary condition is not satisfied, there is a significant difference between the generalized Onsager model and the simulation results. This underlines the necessity of ensuring that the same boundary conditions are satisfied in the model and the simulations; there could be a difference in the results not only because of model approximations, but also because the boundary conditions are not exactly satisfied.

The axial mass flux, scaled by $((\rho_w \Omega R), (4\mathscr{A}^4(Z/R)/Re))$, is plotted as a function of the normalized radial scale height ξ^* for different stratification parameters and Reynolds numbers for the isothermal sidewall (with energy removal from wall) as shown in figure 18(*a*,*b*,*c*). The flux is scaled in such a manner that the analytical solution is independent of the Reynolds number and aspect ratio, and depends only on the stratification parameter. We have shown the results only for the case where energy is removed at the wall so that the homogeneous temperature boundary condition is maintained, and at the location $\eta = 0.45$, where the axial velocity slip was found to be close to maximum from figure 16. It is observed that the magnitude of axial mass flux is larger when the momentum source is placed within the radial boundary layer at $\xi_s^* = 0.01$, in comparison to the case where the momentum source is outside the radial boundary layer at $\xi_s^* = 0.25$. There is quantitative agreement (with a difference of less than 10 %) between the predictions of the analytical model and the simulations even when the stratification parameter is 0.707, the Reynolds number is 100 and the cylinder length is twice the diameter. We find better agreement for higher aspect ratios, and higher Reynolds numbers and stratification parameters, though the results are not shown here.

https://doi.org/10.1017/jfm.2011.289 Published online by Cambridge University Press

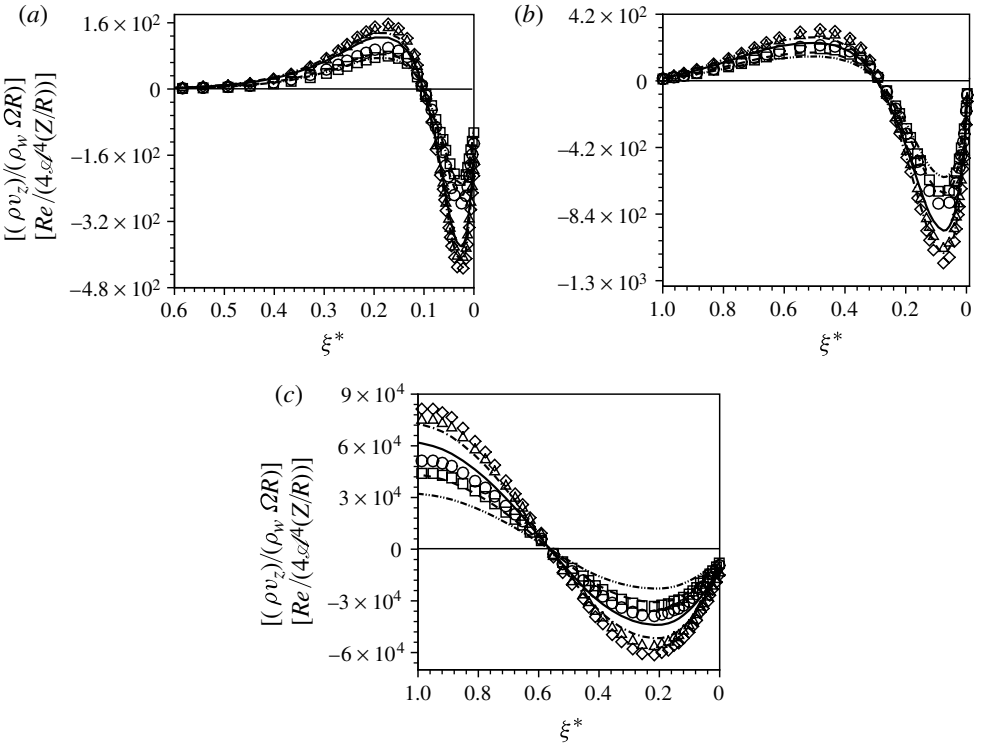


FIGURE 18. Axial mass flux, scaled by $(\rho_w\,\Omega R)$, $(4\mathscr{A}^4(Z/R)/Re)$, as a function of ξ^* for $Z/D = 2$ at the axial location $\eta = 0.45$, for $\mathscr{A} = 3.535$ (a); $\mathscr{A} = 2.121$ (b); and $\mathscr{A} = 0.707$ (c). Flow induced by momentum source at $\eta = 0.5$. Reynolds number Re (for each stratification parameter) $= 10^4$ and 10^2, aspect ratio $Z/D = 2$ and source strength $=$ 0.2. The symbols show the DSMC results for $Re = 10^2$, $\xi_s^* = 0.25$ ($\circ$), $Re = 10^4$, $\xi_s^* = 0.25$ ($\square$), $Re = 10^2$, $\xi_s^* = 0.01$ ($\diamond$), $Re = 10^4$, $\xi_s^* = 0.01$ ($\triangle$). The lines show the generalized Onsager model with slip ($--$) and the Onsager model with slip ($\cdot\cdot--\cdot\cdot$) with source at $\xi_s^* = 0.25$, and the generalized Onsager model with slip ($\cdot-\cdot$) and the Onsager model with slip (—) with source at $\xi_s^* = 0.01$.

8.2. *Mass source/sink*

The secondary flow generated by a mass source/sink, as shown in figure 13(b) has also been studied at different Reynolds numbers and stratification parameters. Results for the stratification parameters $\mathscr{A} = 3.535$, 2.121, 0.707, Reynolds numbers $Re = 10^4$, 10^2, with aspect ratio $Z/D = 2$ and $F^* = 0.2$, are shown in figure 19. The mass source/sink is placed in two different radial locations, one inside ($\xi_s^* = 0.01$) and other outside ($\xi_s^* = 0.25$) the radial boundary layer. Mass is introduced in the flow domain by adding molecules to the system at $\eta = 0.25$ through the circle of radius $10^{-3}R$ which is connected to a pressure bath. Similarly, the mass is removed by removing molecules through a circle of the same radius at $\eta = 0.75$ which is also connected to a pressure bath.

The scaled axial mass flux, non-dimensionalized by $(\rho_w\,\Omega R)(4\mathscr{A}^4(Z/R)F^*/Re)$, is plotted as a function of ξ in figure 19. The flux is scaled in such a manner that the analytical solution is independent of the Reynolds number and aspect ratio, and depends only on the stratification parameter. The results are plotted only at the axial

https://doi.org/10.1017/jfm.2011.289 Published online by Cambridge University Press

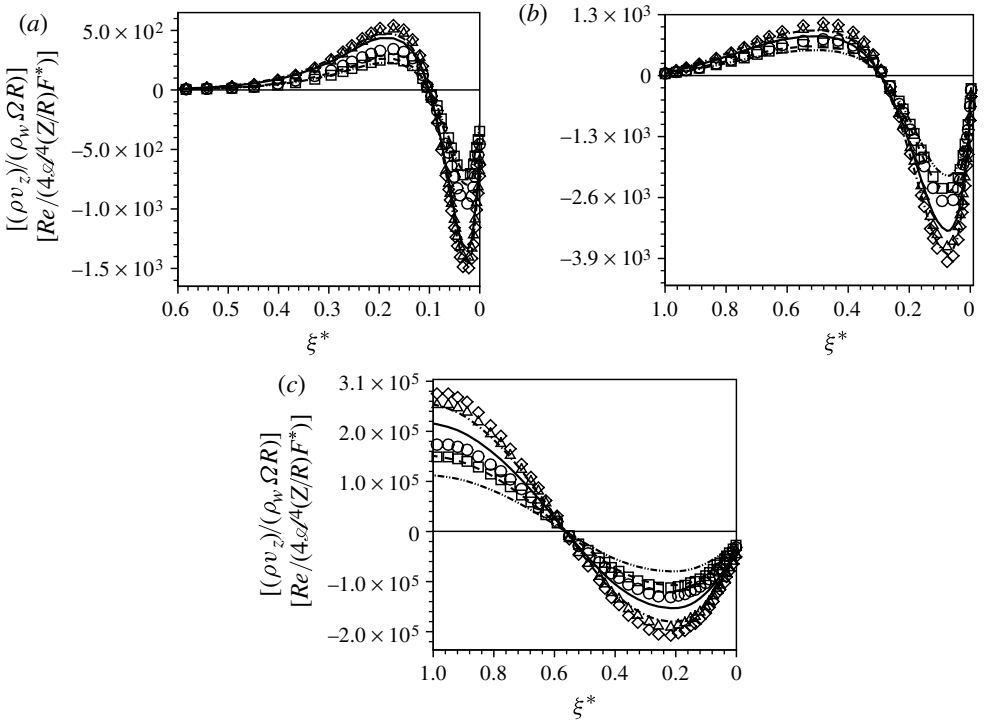


FIGURE 19. Axial mass flux, scaled by $(\rho_w \Omega R)$, $(4\mathscr{A}^4(Z/R)F^*/Re)$, as a function of ξ^* for $Z/D = 2$ and $F^* = 0.2$ at the axial location $\eta = 0.18$, for $\mathscr{A} = 3.535$ (*a*), $\mathscr{A} = 2.121$ (*b*) and $\mathscr{A} = 0.707$ (*c*). Flow induced by a mass source at $\eta = 0.25$ and a mass sink at $\eta = 0.75$. The symbols are simulation results for different Reynolds numbers and radial source locations, $Re = 10^2$, $\xi_s^* = 0.25$ (○), $Re = 10^4$, $\xi_s^* = 0.25$ (□), $Re = 10^2$, $\xi_s^* = 0.01$ (◇), $Re = 10^4$, $\xi_s^* = 0.01$ (△). The lines show the results of the generalized Onsager model with slip with source at $\xi_s^* = 0.25$ (− −), the Onsager model with slip with source at $\xi_s^* = 0.25$ ($\cdot\cdot-\cdot\cdot$), the generalized Onsager model with slip with source at $\xi_s^* = 0.01$ ($\cdot-\cdot$), and the Onsager model with slip with source at $\xi_s^* = 0.01$ (—).

location $\eta = 0.18$, where the axial velocity slip was found to be a maximum from figure 16. The results show quantitative agreement between the DSMC simulations and the analytical results of the generalized Onsager model, provided the velocity slip is incorporated in the analytical solutions, and care is take to ensure that the temperature is a constant at the sidewall. There is agreement to within 10 % even when the Reynolds number is as low as 100, the stratification parameter is 0.707 and the aspect ratio is only 2. The results for higher aspect ratios, not shown here, are in even better agreement with the simulation results. There is a significant difference between the original Onsager model with slip and the simulation results. We have also carried out two further tests, whose results are not shown here for conciseness. When constant temperature boundary conditions are not enforced in the simulations, we find that the difference between analytical and simulation results is more than twice that when the constant temperature boundary conditions are enforced. When the velocity slip is not enforced, there is a much larger difference (30–50 %) between the simulation and analytical results.

https://doi.org/10.1017/jfm.2011.289 Published online by Cambridge University Press

9. Conclusions

It is important to recall the approximations made in the derivation of the generalized Onsager equation for the radial boundary layer, and the generalized Carrier–Maslen equation for the axial boundary layer at the end caps. In both cases, the equations are linearized in the perturbation to the base flow, which is a solid-body rotation. Therefore, these equations are valid only for small secondary flows. The equations are restricted to the limit of high Reynolds number and (length/radius) ratio, but there is no limitation on the stratification parameter. The linear operators in the Onsager and Carrier–Maslen equations are still self-adjoint, and so the eigenfunctions form a complete orthogonal basis set. However, the differential operator depends explicitly on the stratification parameter, and so it is necessary to evaluate the eigenvalues and eigenfunctions numerically.

For the case of mass/momentum/energy insertion into the flow, the separation-of-variables procedure is used, and the appropriate homogeneous boundary conditions are specified so that the linear operators in the axial and radial directions are self-adjoint. The discrete eigenvalues and eigenfunctions of the linear operators are obtained. The solutions for the secondary flows can be determined in terms of these eigenvalues and eigenfunctions.

The major advantage of the present formulation is that it is not restricted to the asymptotic limit of high stratification parameter, even though we have assumed that the Reynolds number and aspect ratio are high. Consequently, the model is not restricted to just boundary layer flows at the curved surface of the cylinder, but is even applicable to situations where the flow domain extends all the way to the centre of the cylinder. Therefore, the model can be used for much slower flows than the original Onsager model, and this provides a way to bridge the existing gap between the Onsager model for very high-speed (high-stratification-parameter) flows, and incompressible flows where the incompressible Navier–Stokes equations can be used. However, the modified Carrier–Maslen model is applicable only to boundary layer flows at the end caps, though even here, there is now no restriction that the stratification parameter should be much greater than 1.

In the second part of the analysis, we compare the analytical results with those of DSMC simulations. This comparison shows that it is necessary to take certain precautions when making a quantitative comparison between analysis and simulations. In the case of wall temperature gradients, it is necessary to ensure that the wall velocity slip and ‘temperature slip’ (difference between gas temperature at the wall and wall temperature) are accurately incorporated in the analytical solutions. In the case of insertion of mass/momentum/energy, it is necessary to accurately enforce the homogeneous boundary conditions at the walls in the simulations, since the analysis assumes homogeneous boundary conditions. When these precautions are taken, we find that there is quantitative agreement (with a difference of less than 10 %) between the predictions of the analytical model and the simulations even when the secondary flow is as large as the 20 % of the base solid-body rotation, the stratification parameter is as low as 0.707, the Reynolds number is as low as 100 and the cylinder length is only twice the diameter. The predictions of the generalized Onsager and Carrier–Maslen models are also significantly better than those of the original Onsager and Carrier–Maslen models (Wood & Morton 1980).

The analytical results have been compared with molecular simulations based on the direct simulation Monte Carlo (DSMC) method, for the secondary flow in a rotating cylinder. Several situations have been considered, including a wall temperature variation with a maximum scaled temperature gradient of 0.2, mass flux at the centre

https://doi.org/10.1017/jfm.2011.289 Published online by Cambridge University Press

of the cylinder with a maximum mass flux (scaled by the holdup and angular velocity) of 0.2, as well as delta function momentum and energy sources within the domain of the flow. Simulations have been carried out for Reynolds numbers as low as 100, stratification parameters as low as 0.707 and aspect ratios as low as 2.

Even for this strong forcing, we find that the analytical solutions are in excellent agreement (error within 10 %) with the results of DSMC simulations even when the stratification parameter is as low as 0.707, the Reynolds number is as low as 100, and for cylinders with length/diameter ratio as low as 2, provided precautions are taken to ensure that the homogeneous boundary conditions assumed in the analytical solutions are accurately reproduced in the simulations. The linear superposition of solutions obtained for inhomogeneous boundary conditions and for internal sources of mass, momentum and energy are also found to be in good agreement with simulations. This shows that the the generalized Onsager and Carrier–Maslen models have excellent predictive capabilities even at relatively low Reynolds number and stratification parameter, and for cylinders of relatively low aspect ratio, provided that care is taken in the specification of boundary conditions. They also represent a significant improvements over the original Onsager and Carrier–Maslen models.

The present analysis also reveals potential difficulties in the continuum modelling approach based on the compressible Navier–Stokes equations. It has already been realized that the continuum equations may not be valid in the central region of a high-speed rotating cylinder, where the density is low and the mean free path is as large as the macroscopic scale distance (from the axis). As discussed in the Introduction, 'artificial boundary conditions' at a fixed inner surface have been formulated to resolve this problem. Our analysis and simulations show that there is substantial slip in the axial velocity at the wall of the cylinder as well; accurate results are not obtained when this slip is not considered in analytical solutions. If continuum Navier–Stokes solutions are to provide accurate results, it is necessary to specify slip boundary conditions at the outer wall as well. Molecular simulations have the distinct advantage that the slip velocity emerges naturally from the particle–wall collision laws, and it does not have to be modelled.

The authors would like to thank the Department of Science and Technology, Government of India, for financial support. We thank the Chairman, Atomic Energy Commission and Secretary, Department of Atomic Energy, Government of India, Shri T. K. Bera, Director, Chemical Technology Group, and Dr A. Chandrashekara, Bhabha Atomic Research Centre, India, for their kind support for the completion of this work.

Appendix. Conservation equations in cylindrical coordinates

The mass momentum and energy conservation equations for an axisymmetric flow in a cylindrical coordinate system are

$$\frac{\partial \rho}{\partial t} + \boldsymbol{\nabla} \cdot (\rho \boldsymbol{v}) = \mathscr{S}_m, \tag{A 1}$$

$$\rho \left(\frac{\partial v_r}{\partial t} + v_r \frac{\partial v_r}{\partial r} - \frac{v_\theta^2}{r} + v_z \frac{\partial v_r}{\partial z} \right) = -\frac{\partial p}{\partial r} + \left[\frac{1}{r} \frac{\partial (r\tau_{rr})}{\partial r} - \frac{\tau_{\theta\theta}}{r} + \frac{\partial \tau_{rz}}{\partial z} \right] + f_r, \tag{A 2}$$

$$\rho \left(\frac{\partial v_\theta}{\partial t} + v_r \frac{\partial v_\theta}{\partial r} + \frac{v_r v_\theta}{r} + v_z \frac{\partial v_\theta}{\partial z} \right) = \left[\frac{1}{r^2} \frac{\partial (r^2 \tau_{r\theta})}{\partial r} + \frac{\partial \tau_{\theta z}}{\partial z} \right] + f_\theta, \tag{A 3}$$

https://doi.org/10.1017/jfm.2011.289 Published online by Cambridge University Press

$$\rho\left(\frac{\partial v_z}{\partial t}+v_r\frac{\partial v_z}{\partial r}+v_z\frac{\partial v_z}{\partial z}\right)=-\frac{\partial p}{\partial z}+\left[\frac{1}{r}\frac{\partial(r\tau_{rz})}{\partial r}+\frac{\partial \tau_{zz}}{\partial z}\right]+f_z, \tag{A 4}$$

$$\begin{aligned}\rho C_v\left(\frac{\partial T}{\partial t}+v_r\frac{\partial T}{\partial r}+v_z\frac{\partial T}{\partial z}\right) = {} & -p(\boldsymbol{\nabla}\cdot\boldsymbol{v})+\tau_{rr}\frac{\partial v_r}{\partial r}+\tau_{\theta\theta}\frac{v_r}{r}+\tau_{zz}\frac{\partial v_z}{\partial z}\\ & +\tau_{r\theta}\left(r\frac{\partial}{\partial r}\left(\frac{v_\theta}{r}\right)\right)+\tau_{\theta z}\left(\frac{\partial v_\theta}{\partial z}\right)\\ & +\tau_{rz}\left(\frac{\partial v_z}{\partial r}+\frac{\partial v_r}{\partial z}\right)+\frac{1}{r}\frac{\partial}{\partial r}\left(rK\frac{\partial T}{\partial r}\right)\\ & +\frac{\partial}{\partial z}\left(K\frac{\partial T}{\partial z}\right)+\mathscr{S}_e,\end{aligned} \tag{A 5}$$

where

$$\boldsymbol{\nabla}\cdot\boldsymbol{v}=\frac{1}{r}\frac{\partial(rv_r)}{\partial r}+\frac{\partial v_z}{\partial z}, \tag{A 6}$$

$$\tau_{rr}=\mu\left(2\frac{\partial v_r}{\partial r}-\frac{2}{3}\boldsymbol{\nabla}\cdot\boldsymbol{v}\right), \tag{A 7}$$

$$\tau_{\theta\theta}=\mu\left(2\frac{v_r}{r}-\frac{2}{3}\boldsymbol{\nabla}\cdot\boldsymbol{v}\right), \tag{A 8}$$

$$\tau_{zz}=\mu\left(2\frac{\partial v_z}{\partial z}-\frac{2}{3}\boldsymbol{\nabla}\cdot\boldsymbol{v}\right), \tag{A 9}$$

$$\tau_{r\theta}=\mu\left(r\frac{\partial}{\partial r}\left(\frac{v_\theta}{r}\right)\right), \tag{A 10}$$

$$\tau_{rz}=\mu\left(\frac{\partial v_r}{\partial z}+\frac{\partial v_z}{\partial r}\right), \tag{A 11}$$

$$\tau_{\theta z}=\mu\left(\frac{\partial v_\theta}{\partial z}\right). \tag{A 12}$$

Equation (A 1) is the mass conservation equation, (A 2), (A 3) and (A 4) are the momentum conservation equations in the r, θ and z directions, and (A 5) is the energy conservation equation.

REFERENCES

ANDRADE, D. A. & BASTOS, J. L. F. 1998 A gas centrifuge thermal hydrodynamical model. In *The Proceedings of Sixth International Workshop on Separation Phenomena in Liquids and Gases, Nagoya*, pp. 92–99.

AOKI, E. & SUZUKI, M. 1985 Numerical studies on gas flow around scoop of a gas centrifuge. In *The Proceedings of Sixth Workshop on Gases in Strong Rotation, Tokyo* (ed. Y. Takashima). pp. 11–29.

BABARSKY, R. J., HERBST, W. I. & WOOD, H. G. 2002 A new variational approach to gas flow in a rotating system. *Phys. Fluids* **14** (10), 3624–3640.

BABARSKY, R. J. & WOOD, H. G. 1990 Approximate eigensolutions for non-axisymmetric rotating compressible flows. *Comput. Meth. Appl. Mech. Engng* **81**, 317–372.

BARK, F. H. & BARK, T. H. 1976 On vertical boundary layers in a rapidly rotating gas. *J. Fluid Mech.* **78**, 749–761.

BERGER, M. H. 1987 Finite element analysis of flow in a gas-filled rotating annulus. *Intl J. Numer. Meth. Fluids* **7**, 215–231.

https://doi.org/10.1017/jfm.2011.289 Published online by Cambridge University Press

BIRD, G. A. 1963 Approach to translational equilibrium in a rigid sphere gas. *Phys. Fluids* **6**, 1518–1519.

BIRD, G. A. 1994 *Molecular Gas Dynamics and the Direct Simulation of Gas Flows*. Clarendon.

BOURN, R., PETERSON, T. D. & WOOD, H. G. 1999 Solution of the pancake model for flow in a gas centrifuge by means of a temperature potential. *Comput. Meth. Appl. Mech. Engng* **178**, 183–197.

BROUWERS, J. J. H. 1978 On compressible flow in a gas centrifuge and its effect on maximum separative power. *Nucl. Technol.* **39**, 311–322.

CHAPMAN, S. & COWLING, T. G. 1970 *The Mathematical Theory of Non-Uniform Gases*. Cambridge University Press.

GUNZBURGER, M. D. & WOOD, H. G. 1982 A finite element method for the Onsager pancake equation. *Comput. Meth. Appl. Mech. Engng* **31**, 43–59.

GUNZBURGER, M. D., WOOD, H. G. & JORDAN, J. A. 1984 A finite element method for gas centrifuge problems. *SIAM J. Sci. Stat. Comput.* **5**.

HARADA, I. 1980*a* A numerical study of weakly compressible rotating flows in a gas centrifuge. *Nucl. Sci. Engng* **73**, 225–241.

HARADA, I. 1980*b* Computation of strongly compressible rotating flows. *J. Comput. Phys.* **38**, 335–356.

HAUSMAN, M. A. & ROBERTS, W. W. 1984 Three dimensional stratified gas flows past an obstacle. *J. Comput. Phys.* **55**, 347–368.

HITTINGER, M., HOLT, M. & SOUBBARAMAYER, B. 1981 Numerical solution of the flow field near a gas centrifuge scoop. In *The Proceedings of Fourth Workshop on Gases in Strong Rotation, Oxford* (ed. E. Ratz). pp. 22–40.

HITTINGER, M., HOLT, M., SOUBBARAMAYER, B. & CORTET, C. 1983 Simulation of gas flow in front of the scoop of a gas centrifuge. In *The Proceedings of Fifth Workshop on Gases in Strong Rotation, Charlottesville, Virginia* (ed. H. G. Wood). pp. 515–532.

JUNG, E. 1983 An analytic solution of the linearized flow equations using the method of eigenvalues. In *The Proceedings of Fifth Workshop on Gases in Strong Rotation, Charlottesville, Virginia* (ed. H. G. Wood). pp. 247–275.

KAI, T. 1983 Analysis of separation performance of gas centrifuge. In *The Proceedings of Fifth Workshop on Gases in Strong Rotation, Charlottesville, Virginia* (ed. H. G. Wood). pp. 1–42.

MATSUDA, T. 1976 A New proposal of gas centrifuge with desirable counter-current. *J. Nucl. Sci. Technol.* **13**, 98–99.

MATSUDA, T. & HASHIMOTO, K. 1978 The structure of the Stewartson layers in a gas centrifuge. Part 1. Insulated end plates. *J. Fluid Mech.* **85**, 433–442.

MATSUDA, T. & NAKAGAWA, K. 1983 A new type of boundary layer in a rapidly rotating gas. *J. Fluid Mech.* **126**, 431–442.

MIKAMI, H. 1973 Thermally induced flow in a gas centrifuge. *J. Nucl. Sci. Technol.* **10**, 580–583.

MIKAMI, H. 1981 Rotating supersonic flow about scoop inlet using an unsteady implicit technique. In *The Proceedings of Fourth Workshop on Gases in Strong Rotation, Oxford* (ed. E. Ratz). pp. 94–112.

MIKAMI, H. 1985 Two dimensional numerical calculation of flow fields about scoop inlet by the piecewise linear method. In *The Proceedings of Sixth Workshop on Gases in Strong Rotation, Tokyo* (ed. Y. Takashima). pp. 67–85.

NAKAYAMA, W. & TORII, T. 1974 Numerical analysis of separative power of isotope centrifuges. *J. Nucl. Sci. Technol.* **11**, 495–504.

OLANDER, D. R. 1981 The theory of uranium enrichment by the gas centrifuge. *Prog. Nucl. Energy* **8**, 1–33.

RIBANDO, R. J. 1984 A finite difference solution of Onsager's model for flow in a gas centrifuge. *Comput. Fluids* **12** (3), 235–252.

ROBERTS, W. W. 1985 Three dimensional stratified gas flows past impact probes and scoops: *N*-body Monte Carlo calculations. In *The Proceedings of Sixth Workshop on Gases in Strong Rotation, Tokyo* (ed. Y. Takashima). pp. 115–132.

https://doi.org/10.1017/jfm.2011.289 Published online by Cambridge University Press

ROBERTS, W. W. & HAUSMAN, M. A. 1988 Hypersonic, stratified gas flows past an obstacle: Direct Simulation Monte Carlo calculations. *J. Comput. Phys.* **77**, 283–317.

ROBLIN, P. & DONEDDU, F. 2000 Direct Monte-Carlo simulations in a gas centrifuge. In *22nd International Symposium on Rarefied Gas Dynamics* (ed. T. J. Bartel & M. C. Gallis). pp. 169–173. American Institute of Physics.

SAKURAI, T. 1981 Linearized thin-wing theory of gas-centrifuge scoops. *J. Fluid Mech.* **103**, 257–273.

VIECELLI, J. A. 1983 Exponential difference operator approximation for the sixth order Onsager equation. *J. Comput. Phys.* **50**, 162–170.

VILLANI, S. (ed) 1979 *Uranium Enrichment*. Springer.

VOLOSCIUK, K. 1981 Application of the vortex transport equations to the calculation of 2 and 3 dimensional extraction chamber flows. In *The Proceedings of Fourth Workshop on Gases in Strong Rotation, Oxford* (ed. E. Ratz). pp. 604–622.

WALZ, A., VOLOSCIUK, K. & SCHUTZ, H. 1983 Numerical investigations of the flow field near a model of a scoop using the vortex transport equations. In *The Proceedings of Fifth Workshop on Gases in Strong Rotation, Charlottesville, Virginia* (ed. H. G. Wood). pp. 425–458.

WOOD, H. G. & BABARSKY, R. J. 1992 Analysis of a rapidly rotating gas in a pie-shaped cylinder. *J. Fluid Mech.* **239**, 249–271.

WOOD, H. G., JORDAN, J. A. & GUNZBURGER, M. D. 1984 The effect of curvature on the flow field in rapidly rotating gas centrifuges. *J. Fluid Mech.* **140**, 373–395.

WOOD, H. G. & MORTON, J. B. 1980 Onsager's pancake approximation for the fluid dynamics of a gas centrifuge. *J. Fluid Mech.* **101**, 1–31.

WOOD, H. G. & SANDERS, G. 1983 Rotating compressible flows with internal sources and sinks. *J. Fluid Mech.* **127**, 299–311.

https://doi.org/10.1017/jfm.2011.289 Published online by Cambridge University Press